Chapter 10
Dynamic Analysis of Train-Bridge System Under Beam Deformation Induced by Concrete Creep and Temperature Effect

In this chapter, the influence of PC beam deformation induced by creep camber and temperature effect on the dynamic responses and running safety of HSR train-bridge system is studied. In this chapter, the influence of PC beam deformation induced by creep camber and temperature effect on the dynamic responses and running safety of HSR train-bridge system is studied. The numerical simulation method for PC beam creep camber is introduced. The vibration responses of train-bridge system excited by creep camber deformation are analyzed, and the safety threshold curves of creep camber under different train speeds are proposed, to ensure the running safety and stability of train vehicles. By numerical simulation and field measurement, the characteristics of bridge sidewise bending and track slab warping deformation under non-uniform temperature field are studied, and their influences on the dynamic response and running safety of the train-bridge system are investigated.

10.1 Introduction

Bridges produce deformations under various factors, such as train loads, long-term creep camber due to prestress action, and temperature effect in non-uniform temperature field. Bridge deformations may change the track performance and deteriorate the track smoothness, which will intensify the vibrations of vehicles, increase the dynamic impact on bridge structures, influence the riding comfort of passengers, and even threaten the running safety of trains. For ballasted-track bridges, the additional track unevenness induced by bridge quasi-static deformation can be adjusted by regulating the ballast thickness and fasteners. While for the HSR bridges with ballastless track, the additional track unevenness can only be adjusted by fasteners, but the adjustment amount is limited. Therefore, the quasi-static deformations of the bridges during post-construction period, especially those induced by the creep camber and temperature effect, should be strictly controlled.

H. Xia et al., *Dynamic Interaction of Train-Bridge Systems in High-Speed Railways*, Advances in High-speed Rail Technology, https://doi.org/10.1007/978-3-662-54871-4_10

The elastic deformations of bridges induced by external loads may disappear quickly after the loads are removed, while the creep camber belongs to a kind of non-reversible quasi-static deformation with the characteristics of long-term growth (Bazant and Baweja 1995; Gardner and Lockman 2001; He 2003; Xia et al. 2011; Duan 2014). As one of the main structural forms, the precast simply-supported PC beams are widely used in HSR lines in China. The creep camber will produce periodic deformations of simply-supported bridges with successively arranged equi-span beams, which will change the geometric state of the track and is harmful to the running safety of train and riding comfort of passengers (Liu 2004; Liu 2005). For HSR bridges, the creep camber of PC beams should be limited (Zheng 2008; Xia 2010; Chai 2012), which is clearly defined in various bridge design codes (BS5400 1990; TB10002.1 2005; TB10002.3 2005; AASHTO 2012).

The quasi-static deformations of the bridge and track structure under the temperature effect may also change the track smoothness state, which will have a great impact on the normal operation of high-speed trains, and even exceed the effects of other loads to become the controlling design factor in some cases (Xia et al. 2006; Zhai 2007; Niu 2008; Zhang 2008; Sun 2013; Tian et al. 2015).

In this chapter, by using the standard 32 and 24 m simply-supported PC beam bridges as examples, the camber and lateral sidewise bending of PC beams and the slab warping deformation of ballastless tracks induced by the concrete creep and temperature effect are studied, and the influences of these deformations on the dynamic responses of train-bridge system and the running safety and stability of high-speed trains are analyzed.

10.2 Influence of PC Beam Creep Camber on Dynamic Responses of Train-Bridge System

10.2.1 Creep Camber of PC Beams

10.2.1.1 Concept of Creep Camber

The aging deformation of concrete materials consists of shrinkage and creep. The shrinkage and creep of concrete will continue to develop after the completion of bridge construction. Although the deformation rate gradually declines, the cumulative deformations increase with time, which will produce additional unevenness of the bridge deck, and further affect the running performance of high-speed trains on the bridges.

Concrete shrinkage is a physical–chemical phenomenon of volume reduction due to the evaporation of free water in cement gels of the concrete, which is not related to the external loads, but dependent on the time. There are mainly five forms of concrete shrinkage deformation: the condensation deformation in casting, the drying shrinkage deformation in hardening, the autogenous-shrinkage deformation,

the shrinkage deformation caused by temperature drop, and the carbonization shrinkage deformation. The shrinkage of concrete will change the internal forces and deformations of the bridge structure, thus alter the deck profiles.

The creep of concrete refers to the phenomenon that the deformation of concrete member increases with time under constant stress, which is related to the magnitude of stress it suffers from. Under the action of dead loads and prestressing forces, the axial compression and bending moment will occur on the beam section simultaneously, and the creep of the beam at the side with greater pressure is larger than that with smaller pressure. Under this action, the beam segment produces upward or downward convex deflection. The creep of concrete is described by creep coefficient, defined as the ratio of creep strain to elastic strain, which is related to the concrete age, loading time, member size, and working environment of the beam.

For a railway beam, the upward convex deflection induced by the concrete creep is called the creep camber. The large creep camber may change the geometric state of track on the beam, which is harmful to the running safety and riding comfort of high-speed trains, so it must be strictly limited.

The ultimate values for concrete shrinkage strain and creep coefficient are stipulated in the *Code for Design on RC and PC Structures of Railway Bridge and Culvert* (TB10002.3 2005), as shown in Table 10.1.

In addition to the causes of the structure itself, the creep deformation of concrete bridges is closely related to the environment and other factors, so it is very difficult to calculate the creep camber accurately. Ye and Liu (2009) measured the creep coefficients of a (85+135+85) m continuous PC beam bridge with ballastless tracks, and used them to simulate the whole process of construction and operation, and the variations of the deck profile with time were calculated, as shown in Fig. 10.1. In the figure, the curves represent the additional deflections after applying the secondary dead loads (laying tracks 90 days after casting the concrete).

Table 10.1 Ultimate values for concrete shrinkage strain and creep coefficient

Item		Ultimate concrete shrinkage strain ε_{co} ($\times 10^{-6}$)				Ultimate creep coefficient ϕ_{co}			
Theoretical thickness 2*A*/*u*/mm		100	200	300	≥ 600	100	200	300	≥ 600
Age of concrete when the prestress is exerted/d	3	250	200	170	110	3.00	2.50	2.30	2.00
	7	230	190	160	110	2.60	2.20	2.00	1.80
	10	217	186	160	110	2.40	2.10	1.90	1.70
	14	200	180	160	110	2.20	1.90	1.70	1.50
	28	170	160	150	110	1.80	1.50	1.40	1.20
	≥ 60	140	140	130	100	1.40	1.20	1.10	1.00

Note (1) For pretensioned structures, the concrete age when the prestress is exerted is generally 3–7 d; For post-tensioned structures, it is generally 7–28 d

(2) *A* is the area of concrete section in the calculation, *u* is the periphery contact length between the cross section and the atmosphere

(3) For concrete age and theoretical thickness between the values given in the table, the linearly interpolated values can be adopted

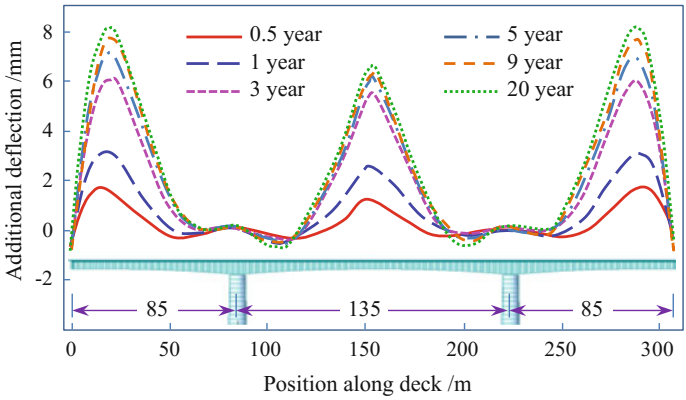

Fig. 10.1 Additional deflection curves of a (85+135+85) m continuous PC beam bridge in various periods

As shown in the figure, the camber and downward deformations of the girders caused by the joint action of concrete shrinkage, creep, and prestress loss increase with time. The additional deflection curves change quickly in the first few years after track laying, while the change gradually becomes slow in the later years.

10.2.1.2 Creep Mechanism and Influence Factors of Concrete

Since the early 1930s, the creep mechanism of concrete has been studied by scholars, and a variety of creep theories have been proposed based on various assumptions. The theories of concrete creep are generally based on the microstructure of the cement paste, such as the viscoelastic theory, the plastic flow theory, the viscous flow theory, the seepage theory, the microfracture theory, and the internal force equilibrium theory, while none of them can explain the creep phenomena satisfactorily. It is generally believed that the elastic deformation of aggregates and cement mortar (namely hydrate skeleton) and the microcracks constitute the initial deformation of the concrete member after loading; with the increase of time, the cement gel gradually produces plastic flows in the internal hydrates skeleton; the cement mortar-aggregate interface and the microcracks in the cement mortar continue to develop and thus cause the continuous and gradual deformation of the concrete member, namely the concrete creep. In addition, the evaporation of water inside concrete can also induce additional drying shrinkage creep of concrete.

The creep of concrete is influenced by various internal and external factors. The internal factors include cement type, concrete mixture ratio, water-cement ratio, size, and manufacturing and curing conditions of concrete members, which influence the microstructural or macrostructural characteristics of concrete. The external factors include the working environment (humidity and temperature), load level,

loading history, and duration of concrete members, which reflect the working characteristics of concrete.

10.2.1.3 Calculation Model of Concrete Creep

Concrete creep is usually described by creep coefficient $\varphi(t,\tau)$, which has two kinds of definition. Assuming $\sigma(\tau)$ the uniaxial constant stress acting on the concrete from time τ, and $\varepsilon_c(t,\tau)$ the generated creep strain at time t, the first definition of creep coefficient is based on the relationship between the creep coefficient and the elastic strain of concrete with 28 d age, expressed as

$$\varepsilon_c(t,\tau) = \frac{\sigma(\tau)}{E_{28}}\varphi(t,\tau) \tag{10.1}$$

where E_{28} is the elastic modulus of concrete with 28 d age.

This definition is adopted in the *Model Code for Concrete Structures* issued by the International Union of Concrete (CEB-FIP 2010), the *Fundamental Code for Railway Bridge and Culvert* issued by the Ministry of Railways of PRC (TB10002.1 2005), and several other codes.

The second definition of creep coefficient is based on the relationship between the creep coefficient and the instantaneous elastic strain of concrete, expressed as

$$\varepsilon_c(t,\tau) = \frac{\sigma(\tau)}{E(\tau)}\varphi(t,\tau) \tag{10.2}$$

where $E(\tau)$ is the elastic modulus of concrete at the moment τ.

This definition is proposed by the *American Concrete Institute Committee* (ACI209 1992), where τ is the standard loading age, which is 7 d for wet curing concrete and 1–3 d for steam curing concrete.

There are several theories to analyze the concrete creep, by considering various influence factors and adopting different calculation methods. In these theories, the mathematical expressions of the creep coefficients are divided into two categories. In the first category, the creep coefficient is expressed as the sum of several partial factors with different properties, such as that used in the early edition of *Code for Design of Highway RC and PC Bridges and Culverts* (JTJ023 1985) issued by the Ministry of Communications of PRC. In the second category, the creep coefficient is expressed as the product of a series of coefficients with different influences on the concrete creep, such as that adopted by the updated version of the *Code for Design of Highway RC and PC Bridges and Culverts* (JTG D62 2004).

In this chapter, the calculation method suggested in the Code JTG G62-2004 is adopted to analyze the creep of simply-supported PC beams. The concrete creep coefficient $\varphi(t, t_0)$ is expressed as

$$\varphi(t,t_0)=\varphi_0\cdot\beta_c(t,t_0) \tag{10.3}$$

$$\varphi_0=\left[1+\frac{1-\mathrm{RH}/\mathrm{RH}_0}{0.46(h/h_0)^{1/3}}\right]\cdot\frac{5.3}{(f_{cm}/f_{cm0})^{0.5}}\cdot\frac{1}{0.1+(t_0/t_1)^{0.2}} \tag{10.4}$$

$$\beta_c(t-t_0)=\left[\frac{(t-t_0)/t_1}{\beta_H+(t-t_0)/t_1}\right]^{0.3} \tag{10.5}$$

$$\beta_H=150\left[1+\left(1.2\frac{\mathrm{RH}}{\mathrm{RH}_0}\right)^{18}\right]\frac{h}{h_0}+250\le 1500 \tag{10.6}$$

where t_0 and t are, respectively, the concrete ages at the time of loading and calculation; φ_0 is the nominal creep coefficient; β_c is the development coefficient of creep after loading; f_{cm} is the average cubic compressive strength of C20–C50 concrete at the age of 28 d (MPa); β_c is a factor related to the average annual relative humidity RH (%), which applies to RH between 40% and 90%; h is the theoretical thickness of the member (mm); RH_0, h_0, t_1 and f_{cm0} are the given coefficients with the values of 100%, 100 mm, 1 d, and 10 MPa, respectively.

10.2.2 Experimental Investigation on PC Beam Creep Camber and Additional Track Unevenness

In the design codes for common railway bridges in China, neither the limit nor the explicit calculation method is proposed for the creep camber of PC beams. For early PC beams, because they were allowed to bear higher pressure stress in the service stage, and to speed up the equipment turnover, higher amount of cement was used and too sooner tensioning was conducted, and very big creep cambers emerged. For example, at the third 31.7 m simply-supported span of the K419 Bridge on the Tianjin–Pukou Railway Line, the maximum cambers of the four pieces of T-beams were measured as 135 mm, 118 mm, 113 mm, and 79 mm, respectively. Similarly, at the 38th span of the Shahe Bridge on the Tianjin-Qinhuangdao Railway Line, the maximum camber of the 31.7 m simply-supported PC T-beam reached 164 mm. According to the investigation, the average value of creep camber for the 32 m PC beams on common railways is about 60 mm. Due to the creep camber of beams, the ballast thickness of the track becomes insufficient and difficult to adjust, which causes the replacement of some beams and great economic losses.

In the *Code for Design of High Speed Railway* (TB10621 2014), the vertical residual creep and deformation of PC beams after track laying is restricted. For ballasted deck, the limit is 20 mm. For ballastless deck, when $L \le 50$ m, the limit

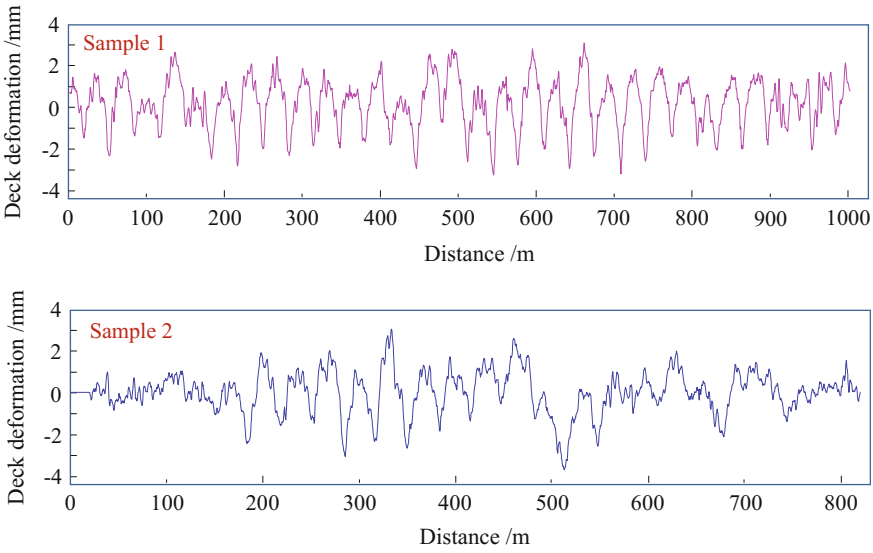

Fig. 10.2 Measured deformation curves caused by creep cambers of successively arranged PC beams

is 10 mm; when $L > 50$ m, the limit is $L/5000$, but not more than 20 mm, where L is the bridge span.

The CARS (China Academy of Railway Science) measured the creep cambers of 32 m simply-supported PC box-beams (43 spans in total) on the Beijing-Shanghai HSR line in 2013, which had served for more than two years by then. Shown in Fig. 10.2 are two typical samples of deformation curves measured at bridge decks, which reflect the joint influence of bridge cambers and uneven settlements. The curves exhibit obvious periodic waves. Analysis results show that they were mainly caused by the creep cambers of successively arranged 32 m PC beams (Li et al. 2014).

When the uneven settlements of piers are removed, the actual creep camber amplitudes of the beams are obtained and listed in Table 10.2.

The bridge deformation caused by the concrete creep produces the additional unevenness of the track on the bridge. For the simply-supported bridge with successive equi-span arrangement, the additional unevenness of the track structure is also periodic.

The CARS measured the track profiles on the Beijing-Shanghai HSR line and obtained the vertical and alignment irregularities of the left and right rails. Shown in Fig. 10.3 are the measured track irregularities of an 800 m section (from mileage K264.4 to K263.6) (Li et al. 2014).

Due to the successive arrangement of 32 m simply-supported PC beams, the amplitude of vertical track irregularity increases significantly with the obvious

Table 10.2 Distribution of creep camber amplitudes measured at the bridge

Creep camber amplitude (mm)	Number of spans	Percentage (%)
1.5–2.0	1	2.33
2.0–2.5	3	6.98
2.5–3.0	4	9.30
3.0–3.5	6	13.95
3.5–4.0	10	23.26
4.0–4.5	10	23.26
4.5–5.0	6	13.95
5.0–5.5	1	2.33
5.5–6.0	1	2.33
6.0–6.5	1	2.33

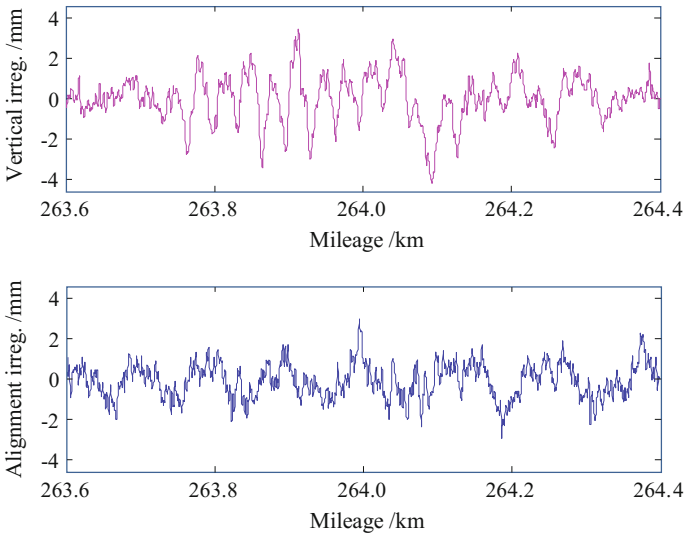

Fig. 10.3 Track irregularities measured on Beijing–Shanghai HSR line

periodic waves, which is consistent with the creep camber curve in Fig. 10.2. The spatial spectra of the track irregularities are analyzed and shown in Fig. 10.4.

It can be seen that in the spectrum of the vertical irregularity, there is a peak appearing near the 32 m wavelength (i.e., the spatial frequency 1/32 m^{-1}), while no peak at this frequency in the alignment irregularity. This shows that the periodic wavelength is mainly induced by the vertical deformations of the beams and the concrete creep is the main cause.

The experimental results prove that the concrete creep indeed affects the track profiles of the bridge. For the successively arranged simply-supported PC beams, the creep camber causes the additional periodic unevenness of the track. When a

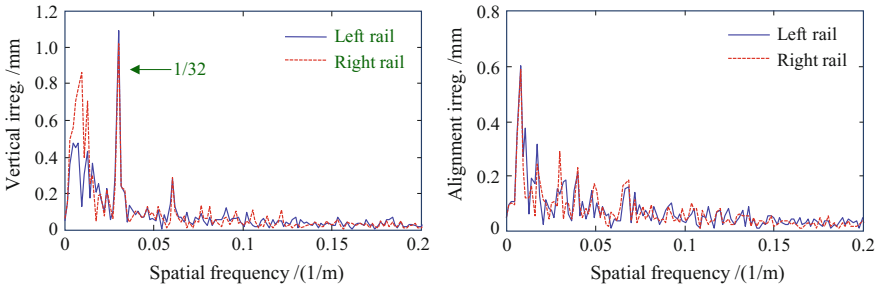

Fig. 10.4 Spatial spectra of the measured track irregularities

train runs on the bridge, such periodic excitation may intensify the vibrations of the train and the bridge and may even induce the resonance of them at certain speeds. Therefore, it is necessary to study the influences of concrete creep cambers on the track irregularity and on the running performance of the train on the bridge.

10.2.3 Analysis of Additional Track Unevenness Induced by PC Beam Creep Camber

With the increase of operation time, the additional deformations of PC beams caused by the concrete creep continue to develop. This additional deformation is gradually transmitted upwards through the track slabs and fasteners, which arouses additional internal forces in the track, causes additional unevenness of the track on the bridge, and even influences the running performance of the train. In order to study this influence, it is necessary to analyze the variation laws of the beam deformation and the additional track unevenness caused by the concrete creep.

10.2.3.1 FE Model of Creep Calculation for Beam-Track System

In China, bridges take a high proportion in HSR lines, which are mainly composed of 32 m simply-supported PC beams, and a few 24 m beams adopted to adjust the span arrangement. Herein, the 32 m and 24 m simply-supported PC box-beams (Design No. (2008) 2322A) are used to study the influence of additional unevenness of track caused by the beam creep cambers.

The CRTSIII ballastless slab track (Fig. 10.5) is the typical track structure with completely independent intellectual property rights in China. It is mainly composed of rail, fastener, PC slab, reinforced self-compact concrete (self-leveling concrete adjustment layer), positioning convex block, intermediate isolation layer (geotextile), and RC base.

The track adopts unit block structure with the size of 2400 mm × 190 mm. Positioning convex block is set for the track slab on the base, and the intermediate isolation layer is applied between the base and the self-leveling concrete layer. The WJ-8C fastener is used.

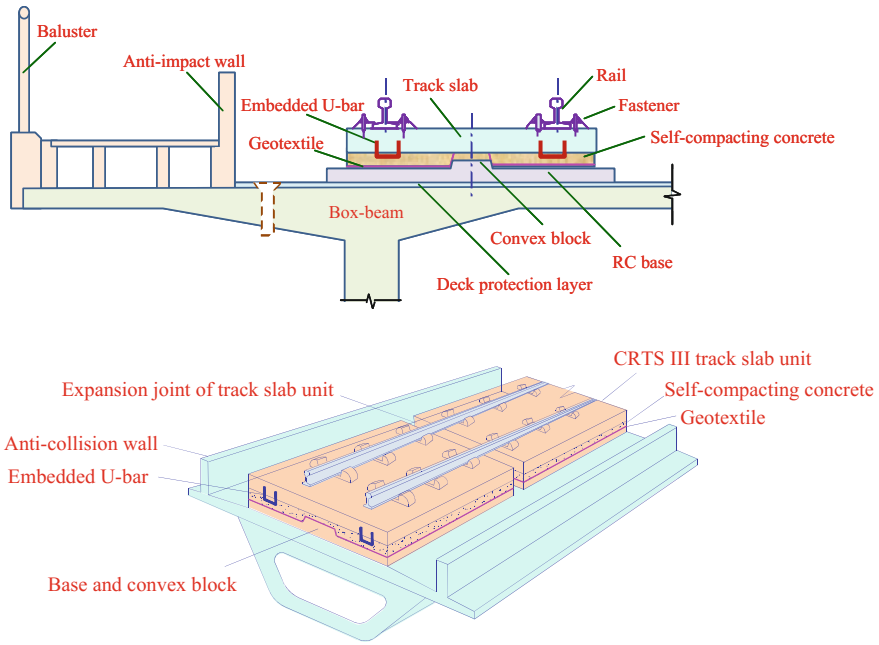

Fig. 10.5 Sketch of ballastless CRTSIII slab track

Shown in Table 10.3 are the layout plans of CRTSIII ballastless track slab units on 32 m and 24 m simply-supported beams, and in Figs. 10.6 and 10.7 are the corresponding specific slab layouts.

It can be seen that this layout allows the edge of the track slab to be justified with the beam end. The parameters of various components of CRTSIII ballastless slab track are listed in Table 10.4.

As shown in Fig. 10.8, the FE model of CRTSIII ballastless slab track on simply-supported beams is established. The model consists of two parts. The left part represents the subgrade, which is used to analyze the additional track unevenness in the beam-subgrade section under the creep camber of the side-span beam. The right part represents the beams, which is used to analyze the additional track unevenness on the beam including the connection section between the beams. In the analysis, it is assumed that the creep laws for all spans are identical.

Table 10.3 Layout plans of CRTSIII track slab units on 32 and 24 m beams (unit: mm)

Bridge span (m)	Slab unit layout	Fastener spacing	Slab joint	Fastener spacing cross slab joint	Fastener spacing cross beam end
32	4925 + 4 × 5600 + 4295	630	70	630/620	590
24	5 × 4856	617	80	617	637

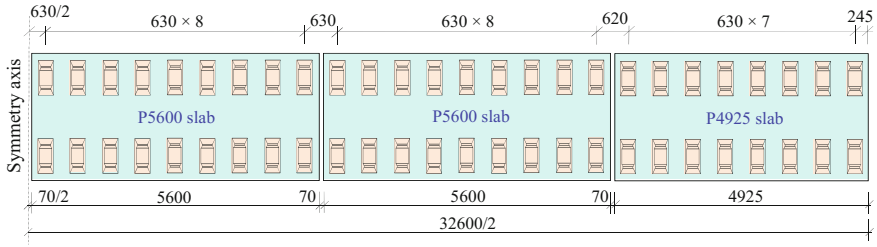

Fig. 10.6 Layout plan of CRTSIII track slab units on 32 m simply-supported beam (unit: mm)

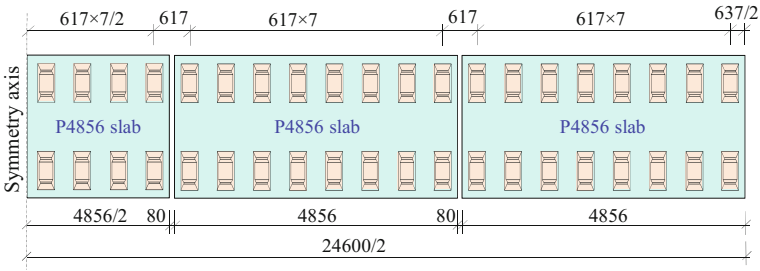

Fig. 10.7 Layout of CRTSIII track slab units on 24 m simply-supported beam (unit: mm)

Table 10.4 Parameters of CRTSIII ballastless slab track

Component	Parameter	Unit	Value
Rail	Section area	cm^2	77.45
	Moment of inertia about the horizontal axis	cm^4	3217
	Moment of inertia about the vertical axis	cm^4	524
	Elastic modulus	MPa	2.1×10^5
Fastener	Longitudinal fastening force/each group	kN	9
	Vertical static stiffness/each group	kN/mm	35
	Lateral static stiffness/each group	kN/mm	50
Track slab	Concrete grade	–	C60
	Density	kg/m^3	2500
	Elastic modulus	MPa	3.65×10^4
Self-compacting concrete	Concrete grade	–	C40
	Density	kg/m^3	2500
	Elastic modulus	MPa	3.4×10^4
Base	Concrete grade	–	C20
	Density	kg/m^3	2500
	Elastic modulus	MPa	2.8×10^4
	Shear bar	HRB335 ϕ28 steel bar, length 0.4 m	
	Supporting stiffness	Subgrade supporting stiffness: 76 MPa/m	

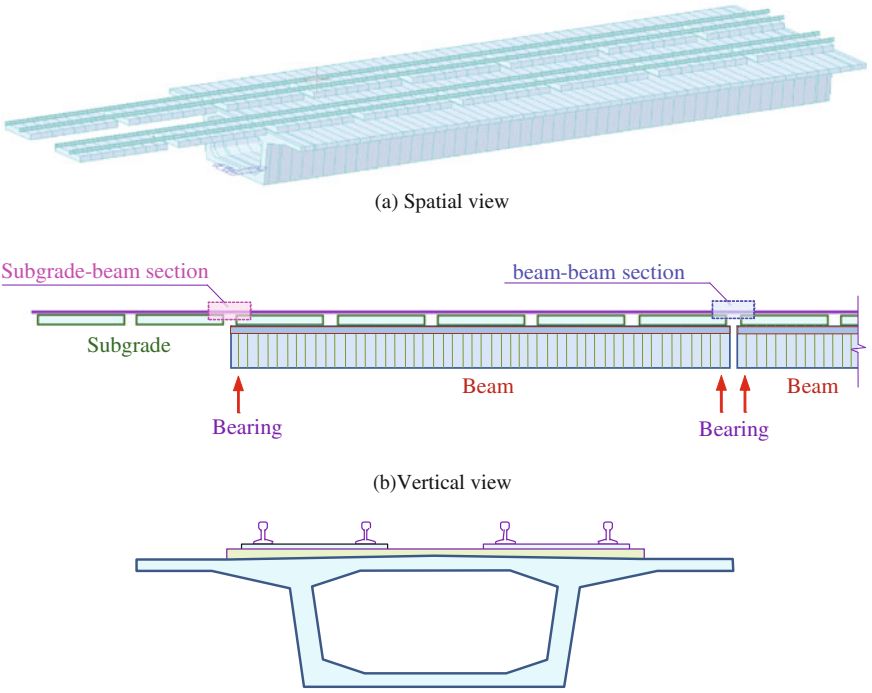

Fig. 10.8 Finite element model of the beam-track system

According to the Saint Venant's Principle, if the asymmetry of the outermost part of the track is ignored, the track deformation in the connection section of beams should be symmetric about the midpoint. Therefore, it is only needed to apply symmetry constraints on the right-side nodes of the model, by releasing the vertical displacement of the node and restricting the remaining DOFs. Thus, in the analysis, only one simply-supported beam is used to simulate the bridge.

According to the characteristics of CRTSIII ballastless slab track, some simplifications are adopted for the simulation of bridge track system:

(1) Due to the connection by embedded steel U-bars, the track slab and the self-compacting concrete layer can work together, so they are simplified as an equivalent slab.
(2) The geotextile between the self-compacting concrete layer and the RC base is modeled as a discrete compression spring with an equivalent stiffness of 400 MN/m^2. Because the creep only induces the vertical additional unevenness of the track, the compression spring is set on the center of the equivalent slab.
(3) The secondary dead load is adopted as 14.385 t/m.
(4) The prestressing loads are applied according to the actual arrangements of prestressing tendons in the beam.

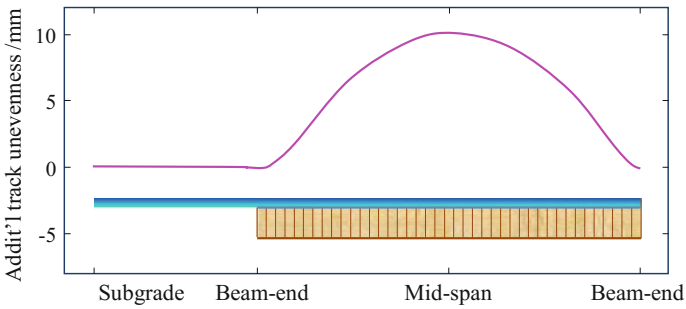

Fig. 10.9 Additional track unevenness caused by creep of simply-supported beam

10.2.3.2 Additional Track Unevenness Caused by Beam Creep

Based on the established analytical model and the assumed beam creep camber of 10 mm, the additional track unevenness caused by the creep of the simply-supported beams is calculated (Fig. 10.9).

It can be seen that due to the continuity of the track, the additional track unevenness curves in the subgrade-beam section and beam-beam section transit smoothly. The additional unevenness curve between the two beams shows a smooth break angle. Since the fastener stiffness (35 kN/mm) and the equivalent compression spring stiffness (400 MN/m^2) of the geotextile are very large, the maximum value of the track additional unevenness appears at the mid-span of the beam, which is approximately equal to the creep value of the beam-body.

10.2.3.3 Effects of Concrete Age and Track Laying Time

Concrete creep is affected by the loading age of the member. The dead loads on the simply-supported PC beam include two types: (1) the deadweights of the beam-body, secondary pavement, and accessory deck facilities; (2) the prestressing force applied on the beam by the prestressing tendons. To study the influence of concrete age on the creep of PC beams, the curing ages of concrete when applying prestressing forces are set as 7 d, 10 d, 14 d, and 21 d, respectively.

From applying prestressing forces on the beam, via beam erecting, to track laying, there is a time interval called track laying time. Only the beam creep after track laying can produce additional track unevenness. The positive moment generated by secondary loads can offset some of the negative moments caused by the creep camber due to the prestressing forces. Therefore, the *Code for Design of High-speed Railways* (TB10621 2014) requires that the accessory facilities be installed as early as possible before laying tracks. In the following analysis, it is assumed that the bridge accessory facilities are installed 20 days before laying the track, and the track laying times (the concrete age when the track is laid) are, respectively, 30 d, 60 d, 180 d, and 360 d.

The analysis results show that the normalized curves of the additional track unevenness under different track laying times are almost the same. Therefore, in the following analysis, it is assumed that the additional unevenness curve of the track is identical to the creep camber curve of the beam, and the amplitude increases with the creep development.

The maximum amplitudes of additional track unevenness for the 32 m and 24 m beams under various curing durations, track laying times, and operation periods after track laying are calculated, and the results are listed in Tables 10.5 and 10.6, respectively.

In the tables, the underlined negative values show that the beam develops negative creep in the early periods after track laying. This is because the moments produced by the secondary loads are opposite to those by prestressing forces, thus the tensile stress of the upper beam edge is reduced, which is equivalent to unloading of the upper edge concrete. The deformation recovery of concrete beams after unloading includes two parts: the immediate elastic recovery ε_{ce} and the elastic aftereffect ε_{cr} recovering gradually with time. Besides, there remains the residual deformation ε_{re}. Under the influence of elastic aftereffect, the creep due to unloading of secondary loads will be gradually recovered, so the negative creep growth appears.

It can be observed that the influence of beam creep on track smoothness is long-standing. Even after 5 years, the additional track unevenness can still develop by 1–2 mm. According to the *Code for Design of High speed Railways* (TB10621 2014), the residual creep of 32 m and 24 m simply-supported PC beams after laying the track should be no more than 10 mm, while the bold italic values in the tables are beyond the limit.

Shown in Figs. 10.10 and 10.11 are the influence of concrete curing duration M_d and track laying time L_d on the final deformation, where the final deformation refers to the additional unevenness of the track caused by beam creep after 20 years of service period.

The following conclusions can be drawn from the above analyses:

(1) Under the same working conditions, the additional track unevenness caused by 32 m beam creep is larger than that by 24 m beam. Under the same curing duration, longer concrete age before track laying is needed for 32 m beam to control the final deformation.
(2) Additional track unevenness decreases with the curing duration and the track laying time, and the latter has a larger influence. Concrete creep develops quickly in the early stage of loading, so the additional track unevenness can be reduced by delaying the track laying time, to release as much as possible the creep before laying track.

Table 10.5 Maximum amplitudes of additional track unevenness on 32 m beam under various conditions (unit: mm)

Curing duration/d	Track laying time/d	Operation period after track laying							
		3 months	6 months	1 year	2 years	5 years	10 years	15 years	20 years
7	30	4.51	6.96	9.54	***12.36***	***16.56***	***18.60***	***19.25***	***19.62***
	60	3.27	5.28	7.63	***10.43***	***14.67***	***16.75***	***17.42***	***17.81***
	180	0.79	1.76	3.41	5.88	9.72	***11.67***	***12.32***	***12.72***
	360	**−0.17**	0.32	1.52	3.55	6.78	8.48	9.10	9.50
10	30	4.16	6.43	8.83	***11.45***	***15.35***	***17.24***	***17.84***	***18.18***
	60	2.98	4.83	7.00	9.60	***13.52***	***15.45***	***16.06***	***16.42***
	180	0.65	1.53	3.06	5.34	8.90	***10.70***	***11.31***	***11.68***
	360	**−0.23**	0.20	1.30	3.17	6.16	7.74	8.31	8.68
14	30	3.84	5.96	8.19	***10.63***	***14.26***	***16.02***	***16.57***	***16.89***
	60	2.72	4.43	6.44	8.85	***12.46***	***14.28***	***14.85***	***15.18***
	180	0.53	1.33	2.73	4.86	8.16	9.83	***10.39***	***10.73***
	360	**−0.29**	0.09	1.09	2.83	5.60	7.06	7.59	7.93
21	30	3.49	5.43	7.48	9.71	***13.00***	***14.65***	***15.15***	***15.44***
	60	2.43	3.99	5.82	8.02	***11.31***	***12.93***	***13.44***	***13.74***
	180	0.40	1.10	2.37	4.30	7.31	8.83	9.33	9.64
	360	**−0.36**	**−0.04**	0.86	2.43	4.95	6.27	6.75	7.06

Table 10.6 Maximum amplitudes of additional track unevenness on 24 m beam under various conditions (unit: mm)

Curing duration/d	Track laying time/d	Operation period after track laying							
		3 months	6 months	1 year	2 years	5 years	10 years	15 years	20 years
7	30	2.58	3.96	5.41	7.00	9.32	***10.47***	***10.83***	***11.05***
	60	1.72	2.78	4.05	5.59	7.93	9.08	9.45	9.67
	180	0.56	1.13	2.06	3.43	5.55	6.64	7.01	7.23
	360	0.04	0.35	1.03	2.16	3.95	4.89	5.23	5.45
10	30	2.39	3.67	5.02	6.50	8.66	9.73	***10.06***	***10.26***
	60	1.74	2.79	4.01	5.45	7.63	8.70	9.05	9.25
	180	0.49	1.01	1.87	3.14	5.11	6.11	6.45	6.65
	360	0.01	0.28	0.91	1.96	3.62	4.49	4.81	5.01
14	30	2.22	3.41	4.67	6.04	8.07	9.06	9.37	9.55
	60	1.60	2.58	3.71	5.05	7.07	8.07	8.39	8.57
	180	0.43	0.90	1.70	2.88	4.71	5.64	5.95	6.14
	360	**−0.03**	0.22	0.80	1.77	3.31	4.12	4.42	4.60
21	30	2.02	3.12	4.28	5.53	7.39	8.30	8.59	8.75
	60	1.45	2.33	3.37	4.60	6.44	7.36	7.65	7.81
	180	0.35	0.78	1.50	2.58	4.25	5.10	5.38	5.55
	360	**−0.06**	0.15	0.68	1.56	2.96	3.70	3.97	4.14

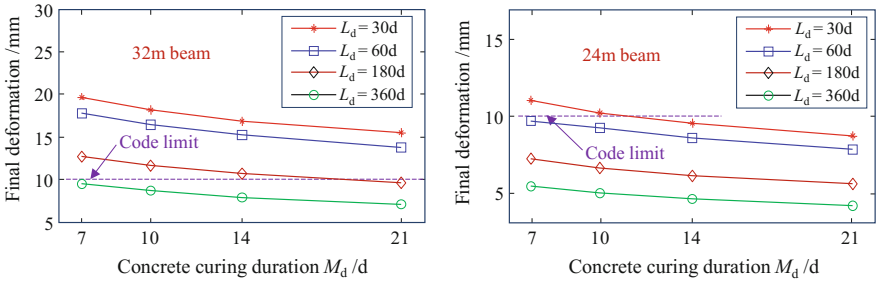

Fig. 10.10 Influence of concrete curing duration M_d on the final deformation under various track laying times

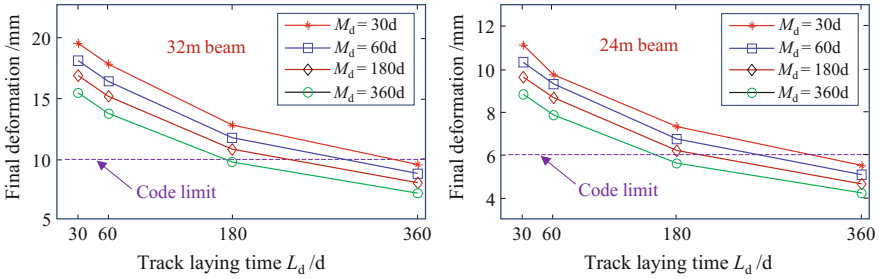

Fig. 10.11 Influence of track laying time L_d on the final deformation under various concrete curing durations

10.2.4 Simulation of Additional Track Unevenness Caused by Beam Creep Camber

In dynamic analysis of train-bridge system, the continuous additional track unevenness is needed, while the calculated results by the FE method are for a series of discrete points, so it is necessary to fit them to form a continuous curve. If the additional track unevenness curves caused by beam creep can be defined by the determinative shape with variable amplitudes, the normalized unevenness curves can be adopted for further analysis.

As shown in Fig. 10.12, the left part of the model is the subgrade and the right part is the simply-supported PC beams. The additional track unevenness curves caused by bridge creep are fitted in three sections, namely the subgrade-beam section, the beam section, and the beam-beam section. Shown in Fig. 10.13 are the fitted additional track unevenness curves normalized with 10 mm amplitude for 32 and 24 m simply-supported beams.

Due to the cantilevered length over beam-ends and the gap between beams, the real lengths for the 32 and 24 m simply-supported PC box-beams are 32.7 m and

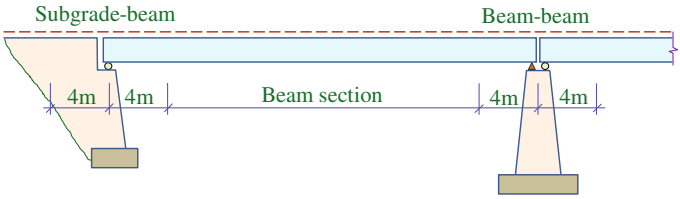

Fig. 10.12 Section partition for fitting simulation of additional track unevenness curves

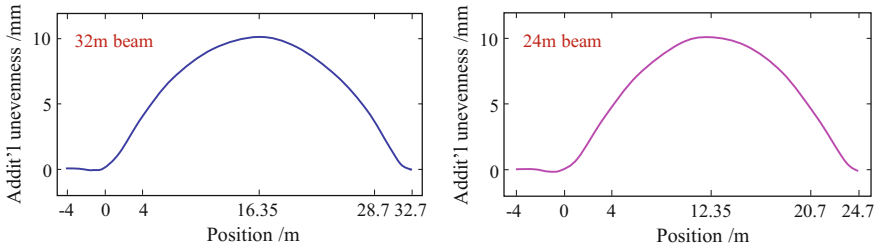

Fig. 10.13 Simulated additional track unevenness curves normalized with 10 mm amplitude

24.7 m, respectively. For easier expression, they are still simply called as 32 and 24 m beams in the following analysis.

Shown in Fig. 10.14 are the additional track unevenness curves of the 10×32 m and 10×24 m bridge with 30 mm creep amplitude. It can be seen that the creep cambers produce a series of concave corners on the additional track unevenness curves at the beam ends, forming a series of successive periodic half-sine waves.

The additional track unevenness curve may excite additional acceleration of the wheel when it moves along the track. Shown in Fig. 10.15 are the additional acceleration curves when the train passes the 10×32 m and 10×24 m bridges with 30 mm creep cambers at the speed of 360 km/h. The curves have the following

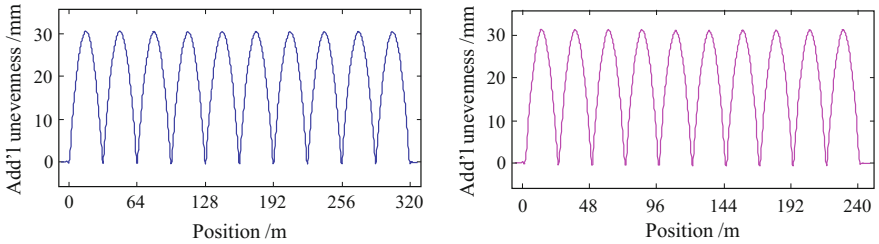

(a) 10×32m bridge (b) 10×24m bridge

Fig. 10.14 Additional track unevenness curves caused by beam creep cambers

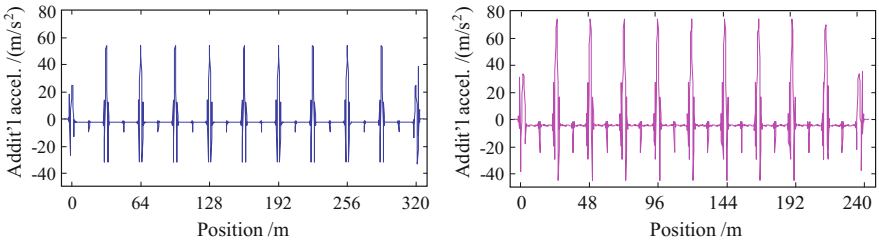

(a) 10×32m bridge (b) 10×24m bridge

Fig. 10.15 Time-histories of additional acceleration caused by additional track unevenness

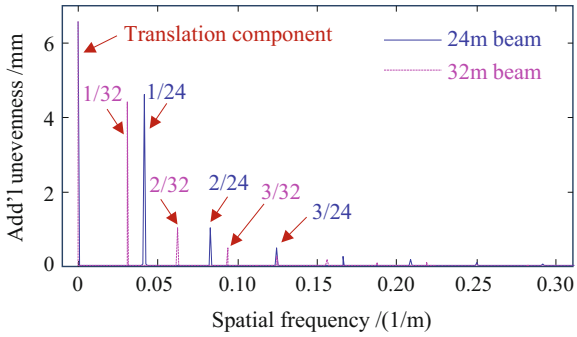

Fig. 10.16 Spatial spectra of additional track unevenness caused by beam creep camber

characteristics: (1) the acceleration peaks appear at the beam-ends; (2) the accelerations at the beam-beam sections are larger than those at the subgrade-beam sections; (3) the accelerations at the beam-ends are much greater than those at the beam centers; and (4) the accelerations on 24 m beams are larger than those on 32 m beams.

To better study the frequency features of the additional track unevenness caused by creep cambers, the additional track unevenness for 50×32 m and 50×24 m simply-supported beam bridges are calculated, and their spatial frequency spectra are analyzed and compared in Fig. 10.16.

As can be seen that in the spatial frequency spectra, only exist components at the frequency points of 0 and $n/32$ (corresponding to the 32 m beam) or $n/24$ (corresponding to the 24 m beam), (n = 1, 2, 3 …). The additional unevenness is composed of the translation component (0 Hz) and the harmonic components with spatial frequencies equal to integral times of $1/L$ (L is the span length), in which the harmonic component corresponding to n = 1 is the most obvious.

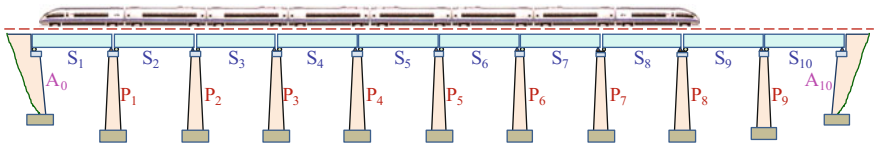

Fig. 10.17 Sketch of the train-bridge model

10.2.5 Influence of Beam Creep on Dynamic Responses of Train-Bridge System

The additional track unevenness caused by the creep cambers of simply-supported bridge with successive equi-span arrangement is periodical, which is equivalent to superposing a long-wave harmonic component on the original track irregularity. In this section, the 10×32 m and 10×24 m simply-supported beam bridges and the Germany ICE3 high-speed train are used to analyze the influences of beam creep on the dynamic responses of the train-bridge system. Shown in Fig. 10.17 is the sketch of the analysis model.

10.2.5.1 Parameters of the Train-Bridge System

The cross section of 32 m simply-supported box-beam is shown in Fig. 10.18, which is also applicable to the 24 m beam, except for the dimensions in brackets. The 6 m-high piers with round-ended section are used, whose bottoms are fixed on the ground. The first vertical natural frequencies for the 32 and 24 m beams are calculated as 4.65 Hz and 5.92 Hz, respectively.

The composition of the ICE3 train is (3M + 1T) × 2, with M denoting the motor-car and T the trailer-car. The parameters of the ICE3 vehicles can be found in Table 6.8 of Chap. 6.

Due to the randomness of track irregularity, when the additional track unevenness is superposed on the original irregularity, the local irregularity will also have

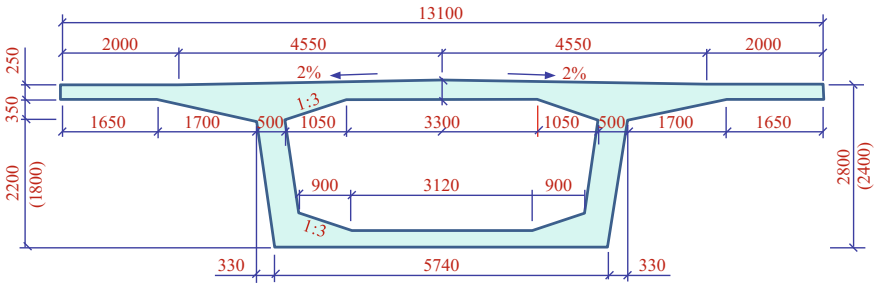

Fig. 10.18 Cross section of the 32 m (24 m) simply-supported PC box-beam (unit: mm)

randomness. Therefore, ten groups of track irregularity samples are generated based on the German low disturbance spectrum. The ten groups of irregularity samples are used to calculate the dynamic responses of the train-bridge system, and the results are averaged to analyze the influence of beam creep cambers.

In simulation analysis of the train-bridge system, the damping ratios for all modes are taken as 0.05, and the integration time step is 0.001 s.

10.2.5.2 Influence of Beam Creep on Car-Body Acceleration

Considering the train speed of 360 km/h, and beam creep amplitude as none and 30 mm, respectively, the whole histories of the train passing through the 10×32 m and 10×24 m simply-supported beam bridges are simulated. Shown in Figs. 10.19 and 10.20 are the calculated car-body acceleration time histories of the fifth vehicle on the two bridges. In the figures, the train position is located by its first wheel-set.

As shown in the figures, the car-body accelerations increase obviously when the additional track unevenness induced by 30 mm creep is considered, and the acceleration curves show the periodicity corresponding to the additional track unevenness.

It can also be seen that the car-body accelerations on the 10×24 m bridge are obviously greater than those on the 10×32 m bridge, and on both bridges, the car-end accelerations are significantly greater than the car-center's, especially when the additional track unevenness induced by 30 mm creep is considered. The frequency spectra of car-body accelerations are also analyzed, as shown in Figs. 10.21 and 10.22.

As can be seen from the figures, compared with the case of none creep, the frequency spectra of the car-body accelerations show predominant peaks at 3.12, 6.25, and 9.38 Hz when the train passes the 10×32 m bridge with 30 mm creep, and show predominant peaks at 4.17, 8.33 and 12.51 Hz when it passes the 10×24 m bridge with 30 mm creep. As analyzed in Chap. 2, the predominant frequencies are related to the span of the beam and the running speed of the train, expressed as

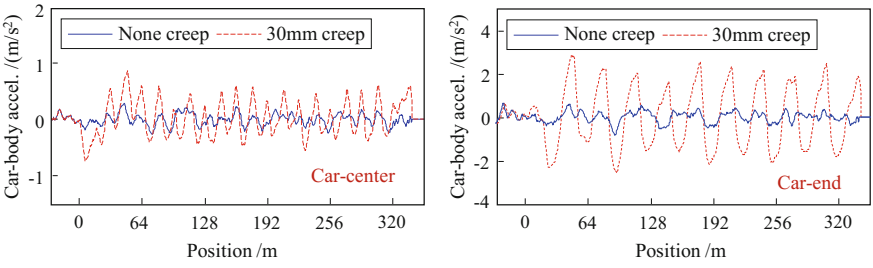

Fig. 10.19 Time histories of car-body acceleration (10×32 m bridge)

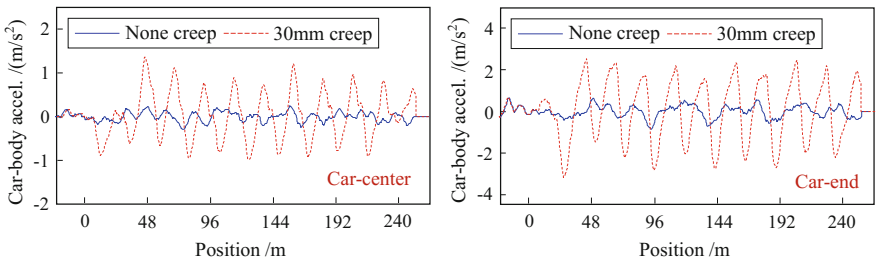

Fig. 10.20 Time histories of car-body acceleration (10×24 m bridge)

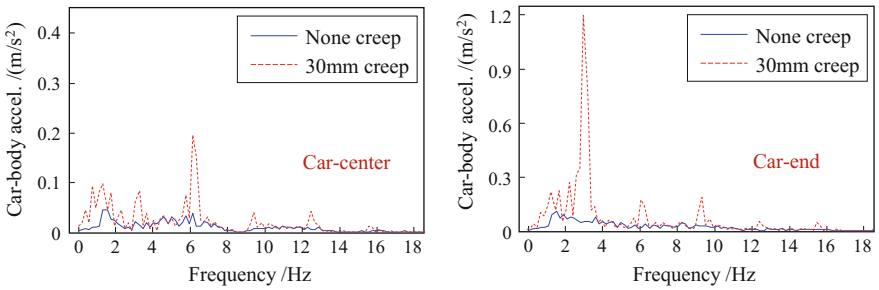

Fig. 10.21 Frequency spectra of car-body acceleration (10×32 m bridge)

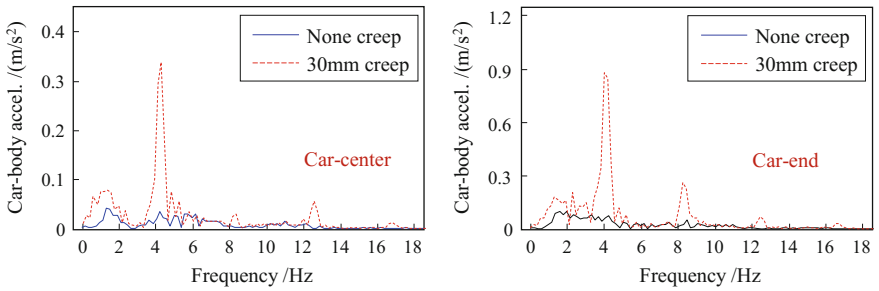

Fig. 10.22 Frequency spectra of car-body acceleration (10×24 m bridge)

$$f = \frac{nV}{3.6L} \quad (n = 1, 2, 3, \ldots) \tag{10.7}$$

where f is the predominant frequency (Hz); V is the train speed (km/h); L is the beam span (m).

The car-end accelerations of the vehicle are further calculated when the train passes the 10×32 m and 10×24 m bridges, considering the train speeds of 160–360 km/h and the beam creep amplitudes of 0–30 mm. Shown in Figs. 10.23 and 10.24 are the spatial distributions and contour graphs of the maximum car-body

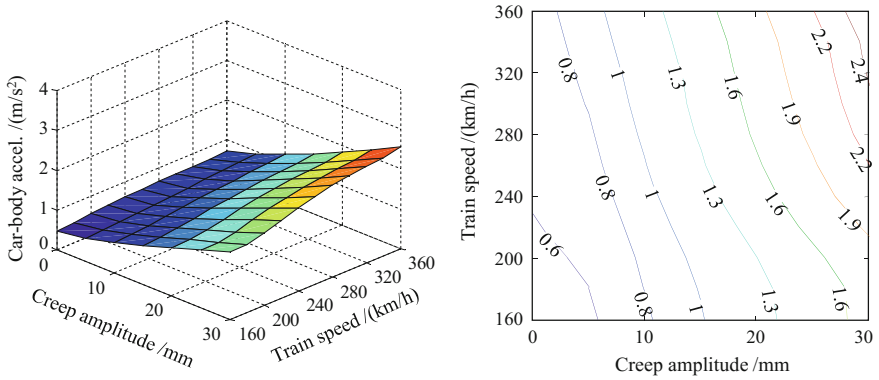

Fig. 10.23 Influence of train speed and creep amplitude on car-end acceleration (10×32 m)

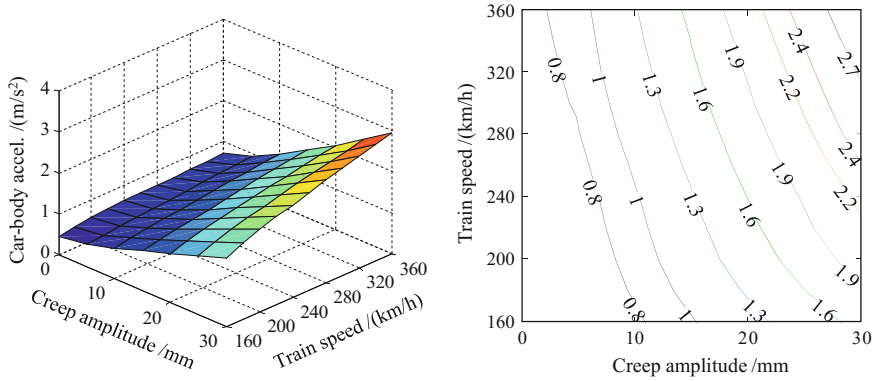

Fig. 10.24 Influence of train speed and creep amplitude on car-end acceleration (10×24 m)

accelerations versus train speed and creep amplitude, where the car-body accelerations are the average values under ten groups of track irregularity samples.

It is obvious that when the train passes the two bridges, the car-body accelerations of the train increase rapidly with train speed and creep amplitude, and the car-body accelerations on the 10×32 m bridge are greater than those on the 10×24 m bridge.

10.2.5.3 Influence of Beam Creep on Train Running Safety

Shown in Fig. 10.25 are the offload factor variation curves of the first wheel-set on the fifth vehicle when the train passes the 10×32 m bridge at the speed of 360 km/h, considering none creep and 30 mm creep of the beams.

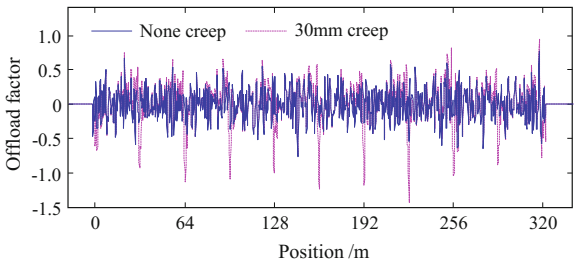

Fig. 10.25 Variation curves of offload factor

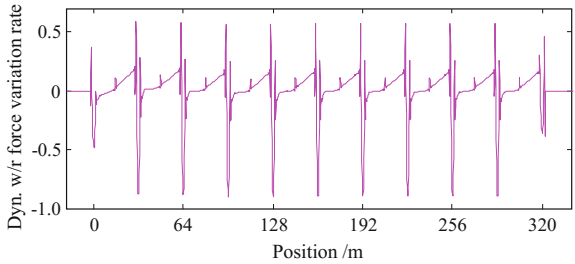

Fig. 10.26 Curves of dynamic wheel-rail force variation rate

To better describe the variations of vertical wheel-rail forces, Fig. 10.26 shows the curves of the dynamic wheel-rail force variation rate, defined as the ratio of dynamic wheel-rail force difference (between the values on creep and none creep beams) to static axle load.

It can be seen that the wheel-rail forces are significantly influenced by the additional track unevenness, especially at the beam-ends, the dynamic wheel-rail force variation rates increase dramatically, being as high as 0.9, while they change little at the beam centers, showing similar variations to the additional track acceleration curves in Fig. 10.15.

For the 10×24 m simply-supported bridge, the wheel-rail forces change more significantly, but the variation curves are similar to those of the 10×32 m bridge, so they are not given.

Compared in Figs. 10.27 and 10.28 are spatial distributions and contour graphs of maximum offload factors versus train speed and beam creep amplitude, when the train passes the beam-end and non-beam-end sections of the 10×32 m bridge and the 10×24 m bridge, respectively.

The following conclusions can be drawn from these figures:

(1) The offload factors increase rapidly with train speed and creep amplitude.
(2) When the train passes the beam-end sections, the offload factors increase more significantly with the creep amplitude than when the train passes non-beam-end Sects.
(3) When the train passes the 10×24 m bridge, the increase trend of offload factors is more obvious than that when the train passes the 10×32 m bridge. For example, in the case with creep amplitude of 30 mm and train speed of

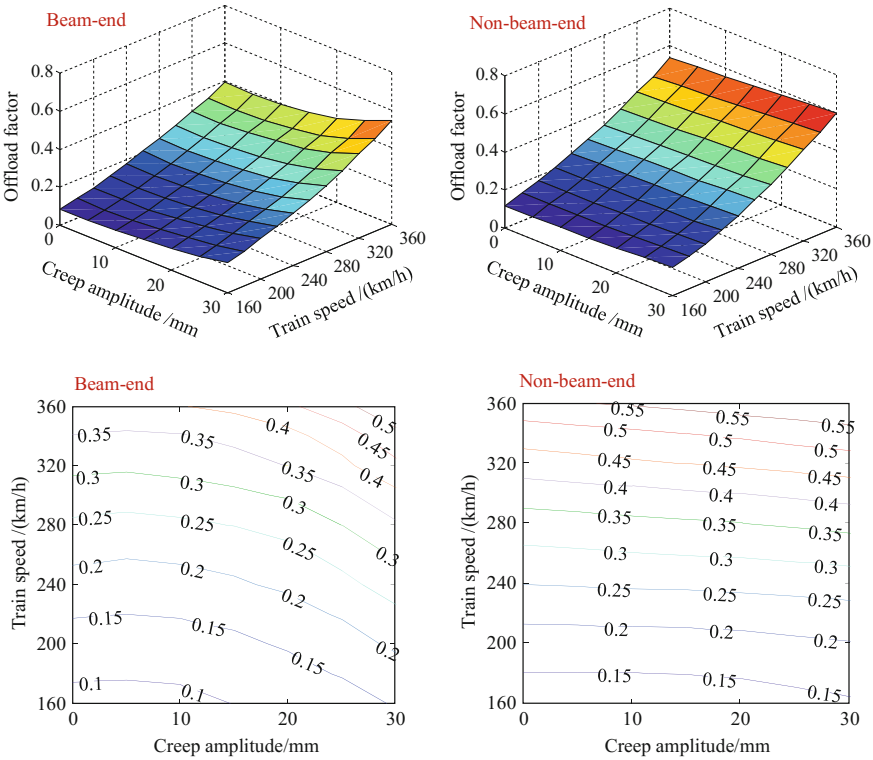

Fig. 10.27 Distributions of maximum offload factors versus train speed and beam creep amplitude (10×32 m bridge)

360 km/h, the offload factors of the train on the 32 m-span bridge increase from 0.393 to 0.545 at beam-ends and from 0.537 to 0.595 at non-beam-end sections. While on the 24 m-span bridge, the offload factors increase from 0.437 to 0.774 and from 0.471 to 0.609, respectively, which are beyond the limit of 0.6.

Shown in Figs. 10.29 and 10.30 are spatial distributions and contour graphs of maximum derailment factors versus train speed and creep amplitude when the train passes the beam-end and non-beam-end sections of the 10×32 m bridge and the 10×24 m bridge, respectively.

In the main trend, the maximum derailment factors increase gradually with train speed and beam creep amplitude. When the train passes the beam-end sections, the derailment factors are more easily affected by the beam creep. Because the derailment factor is simultaneously determined by the lateral force and vertical force between wheel and rail, it is not so much affected by beam creep as the offload factor which is only controlled by vertical wheel-rail force. Therefore, the variations of derailment factors are not elaborated herein in detail.

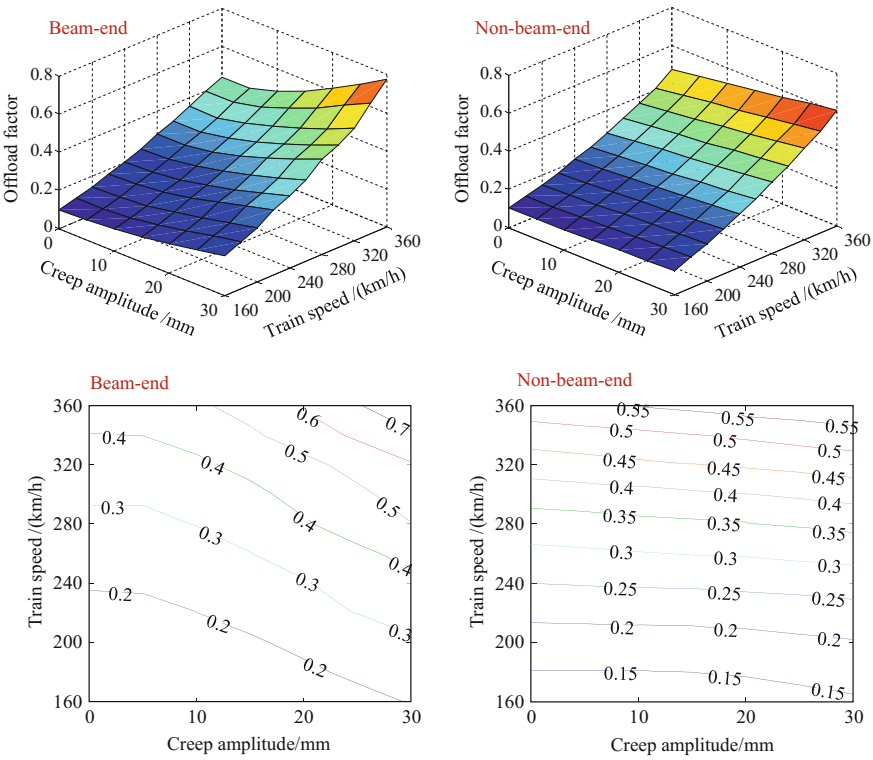

Fig. 10.28 Distributions of maximum offload factors versus train speed and beam creep amplitude (10×24 m bridge)

From the above analysis, it can be seen that under certain beam creep amplitudes and train speeds, the car-body accelerations and offload factors of the train exceed the limits given in the code, which are 1.3 m/s^2 and 0.6, respectively. This further confirms the necessity of studying the influence of beam creep deformation on the dynamic responses of train-bridge system.

Assume the dynamic responses of the train under different track irregularity samples obey the normal distribution, namely, the running safety indices or car-body accelerations have a 50% probability of exceeding the threshold based on the mean values. For the case of 30 mm creep, the maximum car-body accelerations and maximum offload factors under ten groups of track irregularity samples when the train passes the bridge at different train speeds are calculated, and the distributions of them are illustrated in Figs. 10.31 and 10.32.

It can be seen from the figures:

(1) Under low train speeds, the differences among the maximum car-body accelerations and among the maximum offload factors for 10 groups of track irregularity samples are small, and both of them increase with train speed.

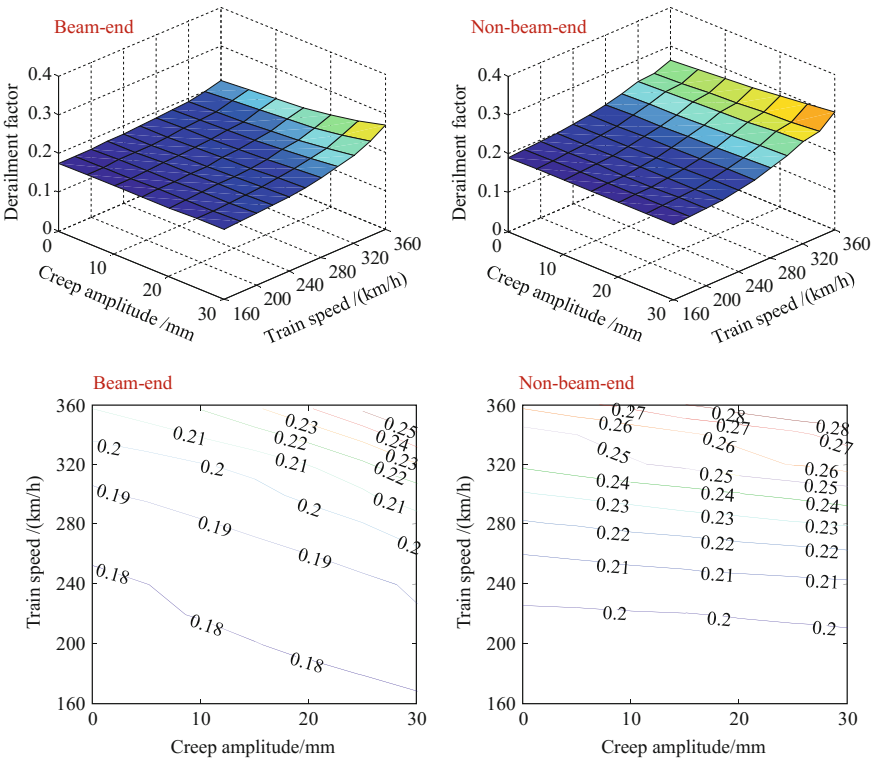

Fig. 10.29 Distributions of maximum derailment factors versus train speed and beam creep amplitude (10×32 m bridge)

(2) The maximum offload factors under different track irregularity excitations show greater discreteness than the maximum car-body accelerations, which is because the offload factors are mainly controlled by the short-wave irregularities, and the short-wave irregularities are more easily affected by the local randomness.

When the train speed is 360 km/h, the offload factors under several groups of track irregularity excitations are beyond the limit of 0.6. Under the tenth irregularity sample, the offload factor reaches 0.93 when the train passes through the 10×24 m bridge, while the average offload factor under the ten irregularity samples is 0.4, indicating that if the safety threshold is based on the average values, the safety factor may be underestimated.

When the train passes through the 10×32 m and 10×24 m bridges under the ten groups of track irregularity samples and various creep amplitudes, the maximum car-body accelerations and offload factors are calculated, based on which the safety and comfort thresholds are proposed, and according to Eq. (9.11), the threshold

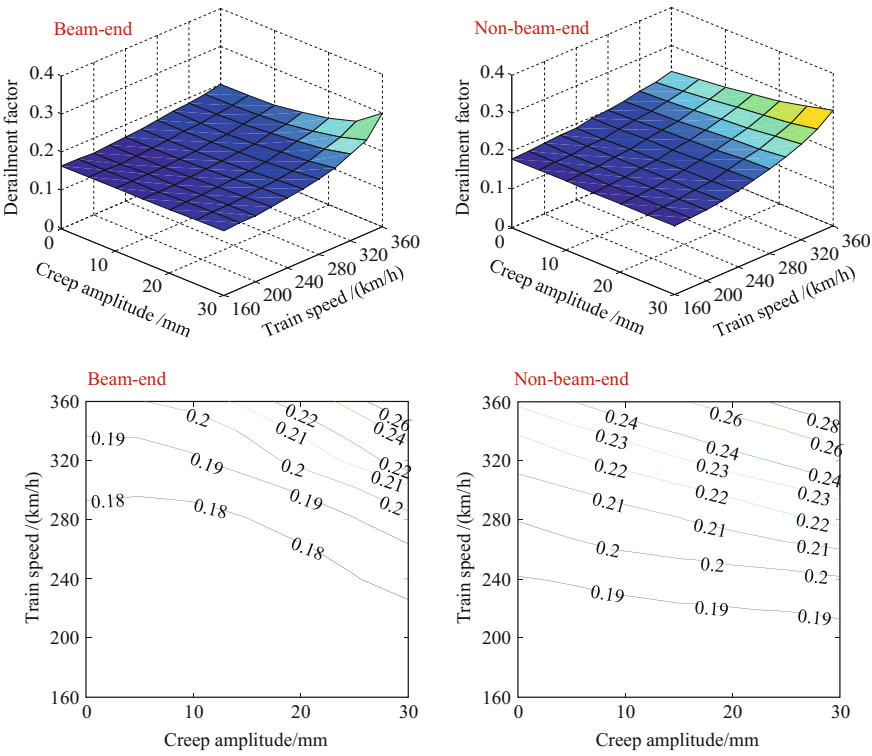

Fig. 10.30 Distributions of maximum derailment factors versus train speed and beam creep amplitude (10×24 m bridge)

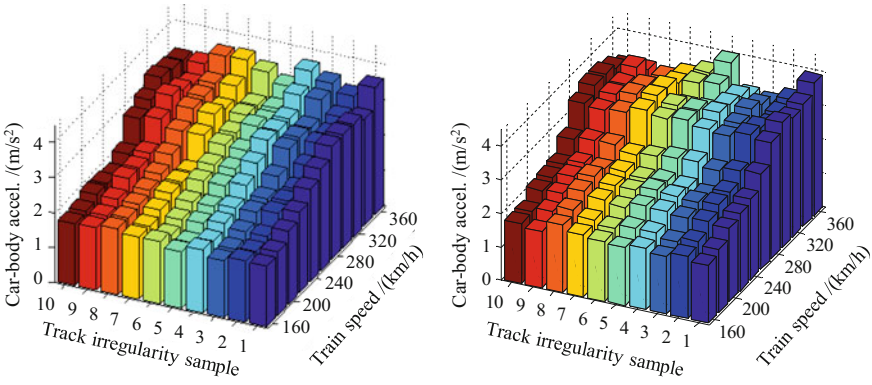

(a) 10×32m bridge (b) 10×24m bridge

Fig. 10.31 Distributions of maximum car-body accelerations under ten groups of track irregularity samples

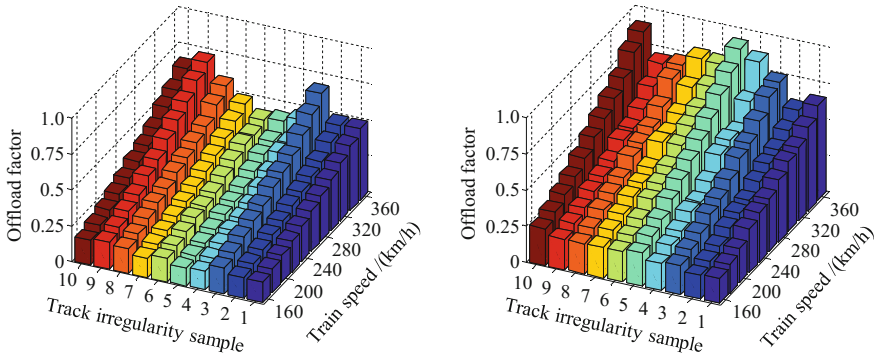

(a) 10×32m bridge (b) 10×24m bridge

Fig. 10.32 Distributions of maximum offload factors under ten groups of track irregularity samples

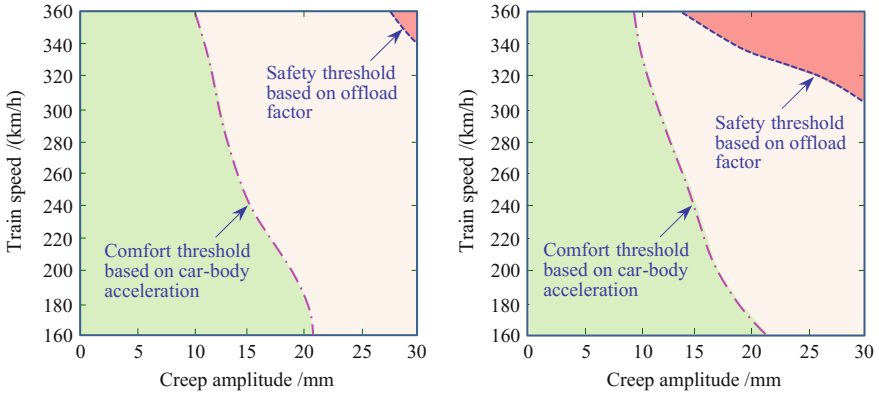

(a) 10×32m bridge (b) 10×24m bridge

Fig. 10.33 Threshold diagrams for running safety and comfort (95% confidence)

curves with 95% confidence are drawn in Fig. 10.33. In the figure, the dash-dotted line is used as the threshold to divide the comfort and uncomfortable zones based on car-body accelerations, and the dotted line is used as the threshold to divide the safety and unsafety regions based on the offload factors.

The following characteristics can be observed from the threshold diagrams:

(1) The safety region of offload factor for the 10×24 m bridge is smaller than that for the 10×32 m bridge, because the 24 m beam produces greater local excitations at the beam-ends.
(2) The safety region defined by acceleration threshold curve is much smaller than that by the offload factor threshold curve, showing that the beam creep affects

the passenger riding comfort (i.e., the car-body acceleration) more than the train running safety (offload factor).

Therefore, for the HSR bridges composed of successive equi-span arrangement PC beams, the additional track unevenness induced by creep cambers should be adjusted timely, to ensure the riding comfort and running safety of the train on bridges.

10.3 Influence of Temperature Deformation on Dynamic Responses of Train-Bridge System

10.3.1 Temperature Deformations of Bridge

For bridges, the temperature deformations consist of two types: the deformation caused by uniform temperature effect, and the deformation caused by the temperature gradient effect.

The bridge deformation under the uniform temperature effect is induced by the seasonal temperature variation in a year, which causes the bridge structures to evenly expand along their longitudinal axes.

The temperature gradient is the sunshine temperature difference due to the solar radiation along the structural height or width within a day (Kyle Buick 1981), whose forming mechanism is shown in Fig. 10.34. When a bridge member is exposed to the sunlight, the temperature in the sunny side becomes higher while in the shady side remains lower. Due to the poor thermal conductivity of concrete materials, most parts of the internal structure are insensitive to the temperature variation, thus forming a large temperature difference. Under the temperature gradient effects, the bridge will generate static deformation. For the ballasted-track beam, only the temperature gradient loads along the beam width need to be considered. While for the ballastless track beam, not only the temperature gradient loads along the beam height and width need to be separately considered, but also their combined effect should be concerned.

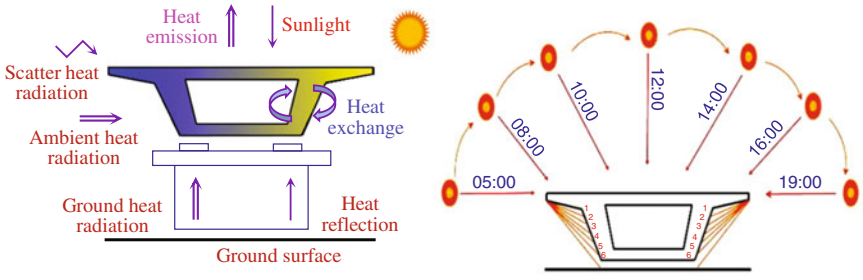

Fig. 10.34 Temperature effects on bridge structure

The uniform temperature effect can be determined by the meteorological data near the bridge site, whose fluctuation range is the difference between the extreme local temperature and the temperature for erection or closure of the bridge.

The range of temperature gradient effect is generally considered that the temperature at the beam top is 5 °C higher than that at the bottom.

According to the *Code for Design on RC and PC Structures of Railway Bridges and Culverts* (TB10002.3 2005), for the box-beam, the sunshine temperature difference curves along the beam height and width are expressed as

$$T_y = T_{01} \times \mathrm{e}^{-cy} \tag{10.8a}$$

$$T_x = T_{02} \times \mathrm{e}^{-cy} \tag{10.8b}$$

where T_{01} and T_{02} are, respectively, the temperature difference amplitudes along the beam height and width, and c is the coefficient of the exponential function, whose values are listed in Table 10.7. The distribution curves of temperature difference are shown in Fig. 10.35. In a practical design, the temperature differences can be calculated according to the temperature difference graph, with the values from 19 to 22 °C along the beam height, and from 12 to 16.5 °C along the width.

The position of the sun changes continuously in a day (and a year), and the heat exchange between the bridge and the environment is very complicated, so the assumed distributions of temperature gradient are usually different from the real temperature field. The track deformation induced by bridge temperature gradient, especially the local track deformation, has a great influence on the running safety of trains. In recent years, the temperature field and the temperature stress of bridge structure have been studied by theoretical analysis and experiments, and the related calculation theories well improved. The results show that the temperature stress in PC box-beams is mainly caused by the temperature difference along the vertical section. At present, there are many researches on the temperature deformations of bridge and track structures (Priestley 1976; Priestley 1978; Liu and DeWolf 2007; Bian 2009; Chen et al. 2010; He et al. 2012; He 2013; Shan 2014), but few attentions are paid to analyze the influence of them on the running safety of high-speed trains (Xia et al. 2006; Zhai 2007; Niu 2008; Zhang 2008; Sun 2013; Tian et al. 2015).

Table 10.7 Parameters for sunshine temperature difference curves along beam height and width

Beam type	Design type	Along beam height		Along beam width	
		$c(\mathrm{m}^{-1})$	T_{01} (°C)	$c(\mathrm{m}^{-1})$	T_{02}(°C)
Ballastless deck	Uni-direction	5	20	none	none
	Bi-direction	7	16	7	16
Ballasted deck	Uni-direction	none	none	7	16

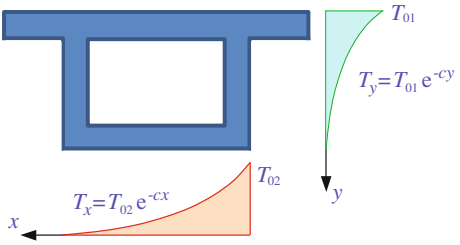

Fig. 10.35 Distribution diagram of temperature difference for box-beam

10.3.2 Numerical Simulation for Sidewise Bending of Beam

As mentioned previously, the temperature effect can cause vertical and transverse deformations of beams. The transverse deformation of the beam is called sidewise bending, which induces the additional transverse unevenness of the bridge. Because the vertical deformation rules of beams caused by temperature effect are similar to those by creep cambers, this section focuses on analyzing the influence of sidewise bending of beams on the train-bridge system.

For the HSR simply-supported bridge with constant-section beams, the sidewise-bending deformation of beam can be simulated with circular curves.

For the 2×32 m simply-supported PC box-beam bridge, the calculation span (distance between the bearings) for each beam is 31.5 m, and the distance between two adjacent beam bearings on the intermediate pier is 1.2 m. If the sidewise-bending amplitude is assumed to be 1, the sidewise-bending deformation is described by two types of circular curves, as expressed by Eq. 10.9a and shown in Fig. 10.36.

$$y_1(x) = \sqrt{\left(\frac{L_1^2}{8A} + \frac{A}{2}\right)^2 - \left(x - \frac{L_1}{2}\right)^2} - \left(\frac{L_1^2}{8A} - \frac{A}{2}\right), \quad (0 \le x \le L_1) \tag{10.9a}$$

$$y_1(\xi) = \sqrt{\frac{L_2^2}{L_1^2}\left(\frac{L_1^2}{8A} + \frac{A}{2}\right)^2 - \left(\xi - \frac{L_1}{2}\right)^2} + \frac{L_2}{L_1}\left(\frac{L_1^2}{8A} - \frac{A}{2}\right), \quad (0 \le \xi \le L_2) \tag{10.9b}$$

where A is the amplitude (maximum value) of the beam sidewise-bending deformation; L_1 is the calculation span of beam; L_2 is the center-to-center distance between the two adjacent beam bearings on the pier. The curves are continuous and first differentiable at the connecting points.

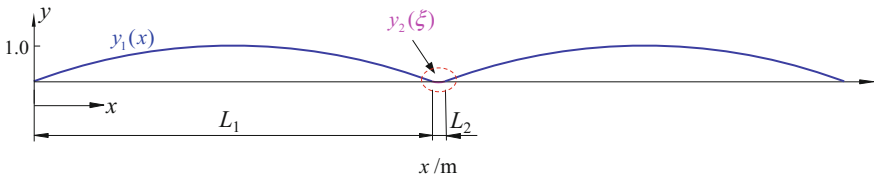

(a) Sidewise-bending curves of two-span simply-supported beams

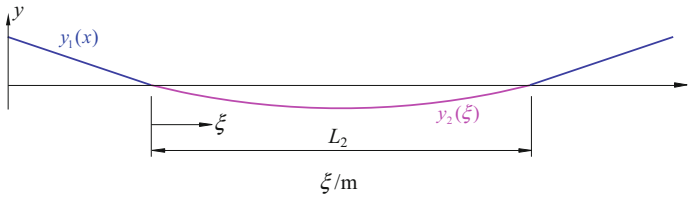

(b) Side-bending connection curve

Fig. 10.36 Simulation curves for temperature sidewise-bending deformation of 2×32 m simply-supported beams

10.3.3 Temperature Warping Deformation of Track Slab and Its Effect on Dynamic Responses of Train-Track System

The CRTSII ballastless slab track used on the Beijing-Shanghai HSR bridges is considered in the analysis. The CRTSII slab track adopts continuous-slab structure. It consists of rail, fastener, PC slab, CA mortar (cement asphalt mortar) layer, PC base (concrete supporting layer), lateral restriction (positioning) block, sliding layer, isolation layer, etc., as shown in Fig. 10.37. The track slabs on the bridge are longitudinally connected, under which are continuous RC base, a sliding layer is set between the base and the protection layer of the beam surface, and restriction blocks are set at the two sides on the base.

The CRTSII track slab is a partially prestressed concrete structure. The standard size of the track slab is 6450 mm × 2550 mm × 200 mm, with "V-shaped" pre-set notches of 4 cm depth at every 0.65 m along the longitudinal direction. Along the direction of the track, the slabs are connected at the ends by 6ϕ20 connecting bars. The section width of the RC base varies from 2.95 m (top) to 3.25 m (bottom). The 30 mm-thick high performance CA mortar is set between the slab and the base as the construction adjustment layer after erection.

The CRTSII track slab is prefabricated in factories with high quality standard. However, there occurred also some problems in construction and operation (Wang et al. 2009), such as the separations of track slab from the CA mortar and the sliding layer under the slab, and the warping and cracking of slab. Han and Sun (2011) found that these problems were related to the track slab temperature: When the track slab is exposed to the sunlight, the surface temperature rises rapidly, while most of

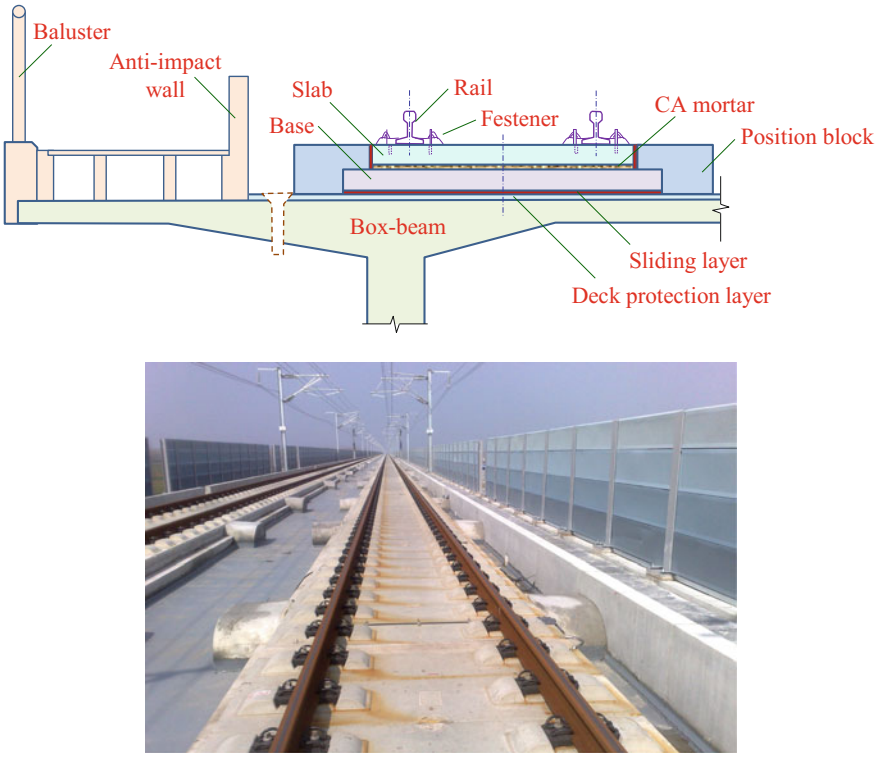

Fig. 10.37 CRTSII ballastless slab track on the bridge

the inner concrete still maintains the original state, as the result, uneven temperature gradient emerges in the slab along the depth.

Two kinds of temperature loads are considered for the track slab, i.e., the uniform temperature variation and the temperature gradient along the depth. The uniform temperature effect causes the longitudinal internal force and deformation of the track, and the temperature gradient along the depth causes the warping deformation of the slab, which leads to the separation between the slab and the CA mortar layer or between the CA mortar layer and the RC base. If the interlayer separation emerges in the construction stage, the track slab will repeatedly beat the CA mortar layer under the dynamic train loads in the operation stage, resulting in the damage of the CA mortar layer and even the failure of the whole track system (Liu and Zhao 2013; Liu et al. 2014).

The temperature field of track slab can be established either by numerical analysis based on the meteorology and heat transfer theories, or by statistical estimation based on a large number of measured data. At present, the researches on the temperature gradient of track slab have been in depth. Liu et al. (2014) investigated the variation characteristics of slab top and bottom temperatures and the temperature gradient, by surveying the slab temperatures of CRTSII tracks on

the Beijing-Shanghai HSR, and based on the measured temperature gradient field, calculated the warping deformation of track slab by FE analysis.

In reality, the variations of uniform temperature and the temperature gradient of track slab usually exist simultaneously, and the temperature deformation of the slab should be under the joint action of the two temperature effects. In order to investigate the temperature deformation of track slabs, a survey was conducted to measure the temperature of track slabs under the field environment, and then the track slab temperature field is simulated by applying nodal temperature loads. Further, the track deformation caused by the temperature loads is used as an additional track unevenness to analyze the dynamic response of the train-track system.

1. **Temperature measurement of track slabs**

On September 11, 2014 and September 13, 2014, the field survey was conducted at the beam yard near the Xiaogan North railway station, in which the temperatures of CRTSII track slabs were measured using the infrared point temperature gun. Shown in Fig. 10.38 are the arrangement of measuring points at slab top and bottom.

The survey was conducted on all measurement points by every half hour, and at each time 3 groups of readings were recorded, which are averaged as the adopted temperatures at that time. Considering several most unfavorable conditions, the measured temperatures of the track slab are analyzed as follows:

When analyzing the temperature gradient of the track slab, the temperature differences at various times in a day are calculated using the measured data of slab top and bottom at different positions. The maximum temperature difference among them and the corresponding slab top and bottom temperatures are adopted.

When analyzing the uniform temperature of the track slab, the maximum temperatures selected from the 9 measuring points on the top and the 6 points on the bottom of the slab in each day are adopted.

Listed in Table 10.8 are the maximum temperature differences and maximum slab temperatures of CRTSII track slab measured in the two-day survey.

2. **Numerical simulation of temperature warping deformation of track slab**

The FE model for temperature warping deformation of track slab is established, as shown in Fig. 10.39.

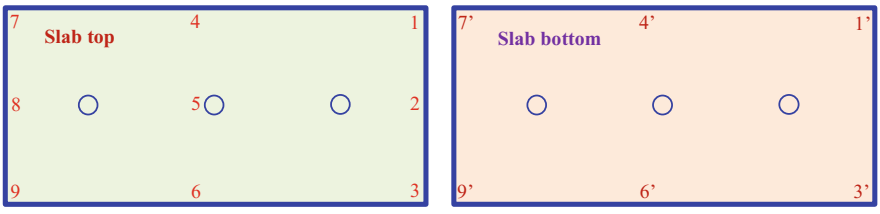

Fig. 10.38 Arrangement of temperature measuring points on the track slab

Table 10.8 Measured temperature results of CRTSII track slab

Date of survey	Maximum temperature difference of slab				Maximum temperature of slab		
	Time	Slab top (°C)	Slab bottom (°C)	Temperature difference (°C)	Time	Slab top (°C)	Slab bottom (°C)
11 Sept.	14:30	33.3	27	+6.3	15:00	35	32.8
13 Sept.	12:00	21.6	8.8	+12.8	12:30	27.6	21.4

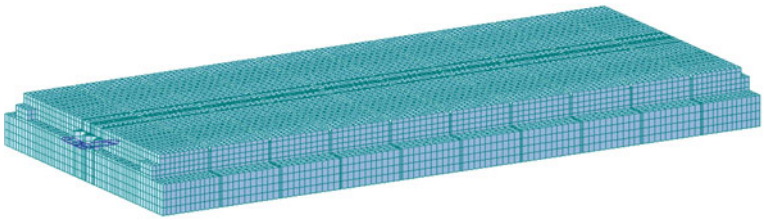

Fig. 10.39 FE model of CRTSII track with single slab

In the model, the track slab, CA mortar layer and RC base are simulated by solid elements; the track slab is supported on the CA mortar layer with nonlinear compression-only springs; the CA mortar layer and the RC base share common points; the connecting bars between the track slabs are simulated by beam elements; the rail is simulated by beam elements, and the fastener by spring elements. The material parameters of CRTSII track components are listed in Table 10.9.

In the calculation, the deadweight of the track slab needs to be considered, but the temperature fields of the CA mortar layer and the RC base can be ignored.

The track slab is loaded by the nodal temperature loads: the initial temperature is the stress-free temperature of the track construction, at which there is neither slab temperature difference nor slab deformation; the final temperature is the measured temperature at the concerned time.

In order to verify the analytical model, the temperature field in Han and Sun (2011), the temperature gradient of −0.275 °C/cm and the temperature difference −5.5 °C between slab top and bottom, is applied on the track slab model. The calculated maximum warping deformation of the slab is 0.4124 mm, which is close

Table 10.9 Material parameters of CRTSII ballastless track

Component	Elastic modulus E (MPa)	Poisson ratio	Linear expansion coefficient (°C)
Rail	2.1×10^5	0.3	1.2×10^{-5}
PC slab	3.6×10^4	0.2	1×10^{-5}
CA mortar	1×10^4	0.34	1.3×10^{-5}
RC base	2.2×10^4	0.2	1×10^{-5}

Table 10.10 Maximum vertical deformations of track slab under the most unfavorable temperature difference conditions

Temperature effect	Initial temperature (°C)	Final temperature (°C)		Temperature difference of track slab (°C)	Maximum vertical deformation of track slab (mm)
		Slab top	Slab bottom		
TG1	20	33.3	27	6.3	0.31
TG2	20	21.6	8.8	12.8	0.53
MT1	20	35	32.8	2.2	0.21
MT2	20	27.6	21.4	6.2	0.23

Note "TG1" denotes the maximum temperature gradient of track slab on the first day; "TG2" the maximum temperature gradient of track slab on the second day; "MT1" the maximum uniform temperature of track slab on the first day; "MT2" the maximum uniform temperature of the track slab on the second day

to the FE calculation value of 0.473 mm and the measured value of 0.45 mm in the reference.

(1) **Analysis of the Most Unfavorable Condition**

According to the temperature survey of the track slab, in the same day, the time with highest temperature is close to the time with maximum top-bottom temperature difference of the slab. The most unfavorable temperature warping deformation of track slab may appear at either of the two moments. Taking the positive temperature difference as an example, the maximum vertical deformations of the track slab under the most unfavorable temperature effects are calculated, and the results are listed in Table 10.10.

It can be seen from Table 10.10 that the maximum vertical deformation of track slab at the maximum temperature (35 °C) is 0.21 mm, which is smaller than 0.53 at the maximum temperature difference (12.8 °C). The higher the temperature difference is, the larger the maximum deformation becomes. Therefore, the most unfavorable temperature warping deformation of track slab occurs at the time with the maximum temperature gradient in a day.

Shown in Figs. 10.40 and 10.41 are, respectively, the temperature warping deformation nephograms of the single-track slab model at the maximum positive and negative temperature gradients. It can be seen that at the maximum positive temperature gradient, the center of the track slab shows an upward warping deformation, while at the maximum negative temperature gradient, the upward warping occurs at the four corners.

(2) **Influence of Uniform Temperature Variation of Track Slab**

Considering the positive and negative temperature gradient conditions, the temperature warping deformations of the track slab are calculated by using different initial temperatures, to analyze the effect of uniform temperature variation.

According to the regional meteorological records of the bridge site, the initial temperature range is set to be −5 °C ∼ 37 °C. For the positive temperature gradient

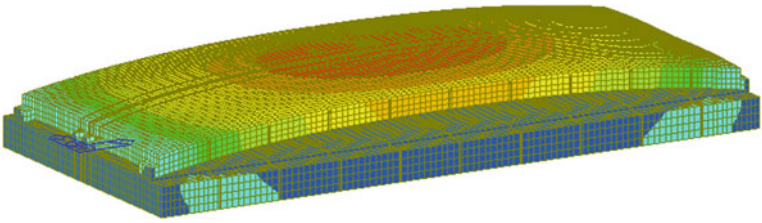

Fig. 10.40 Temperature warping deformation nephogram of track slab at the maximum positive temperature gradient

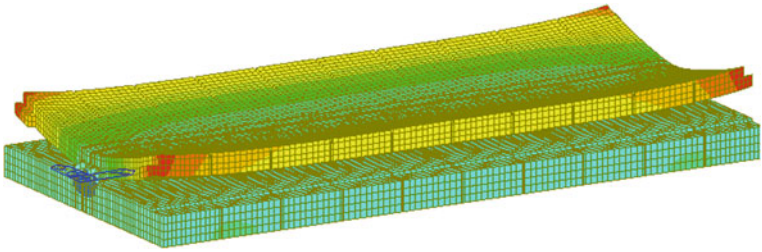

Fig. 10.41 Temperature warping deformation nephogram of track slab at the maximum negative temperature gradient

effect, the temperature difference is 12.8 °C, and the final temperature is 21.6 °C at slab top and 8.8 °C at bottom. For the negative temperature gradient effect, the temperature difference is −5.5 °C, and the final temperature is 30 °C at slab top and 35.5 °C at bottom. The warping deformations of the track slab with respect to different initial temperatures are shown in Fig. 10.42.

Under the positive temperature gradient, the maximum vertical displacement of track slab reaches a minimum value at the initial temperature of 22 °C (slightly higher than the final slab top temperature of 21.6 °C); under the negative temperature gradient, the maximum vertical displacement of track slab reaches a minimum

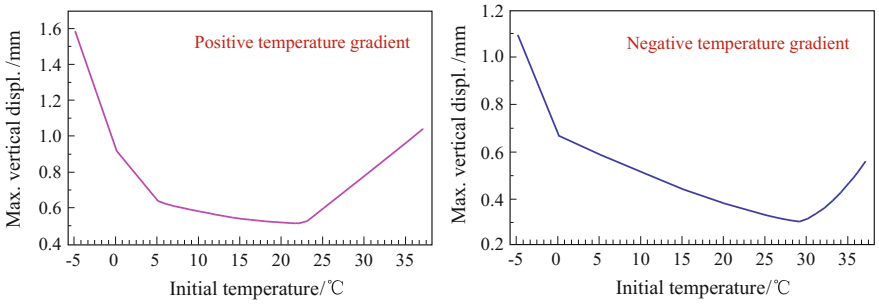

Fig. 10.42 Warping deformations of track slab with respect to different initial temperatures

value at the initial temperature of 29 °C (slightly lower than the final slab top temperature of 30 °C). It shows that the uniform temperature variation has influence on the warping deformation of the track slab. Under the same temperature gradient, the warping deformation of the track slab reaches a minimum value when the initial temperature is close to the slab top temperature.

(3) **Influence of Longitudinal Connection Between Slabs**

To analyze the influence of longitudinal connection on the temperature warping deformation of the track slab, a FE model with three slabs is established, as shown in Fig. 10.43.

In the analysis, the variation curves of the top temperature, bottom temperature, and top-bottom temperature difference of the slab in 24 h given in Han and Sun (2011) are used, as shown in Fig. 10.44.

When the initial temperature is 20 °C, the warping deformations of the single-slab model and the three-slab model in 24 h are calculated, using the temperature loads in Fig. 10.44, and the variation curves of them in 24 h are shown in Fig. 10.45.

It can be seen that at different times in a day, the longitudinal connection plays different roles on the temperature warping deformations of the slab. At 8:00 a.m. and at around 19:00, the temperature differences between slab top and bottom are small, when the warping deformations are increased by the connections. At around 14:00, the positive temperature difference between slab top and bottom reaches maximum, and at around 6:00 a.m., the negative temperature difference reaches maximum, when the warping deformations are decreased.

Fig. 10.43 FE model of CRTSII track with three slabs

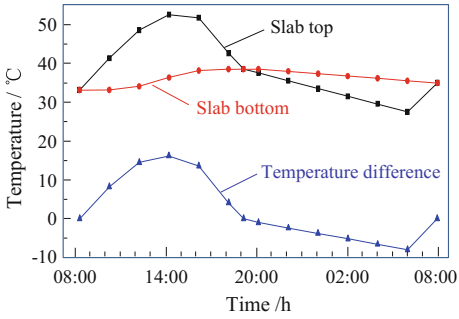

Fig. 10.44 Temperature variation of track slab in 24 h

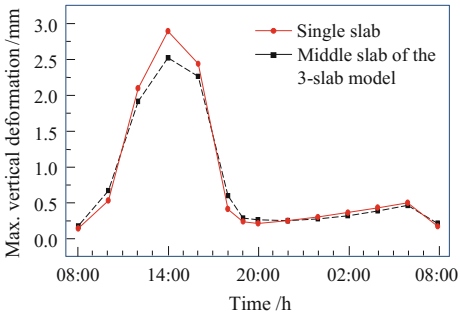

Fig. 10.45 Variations of temperature warping deformation of track slabs in 24 h

For different slab top temperatures at the maximum positive and negative temperature differences, the effects of longitudinal connections on the warping deformations of the track slabs are different. Therefore, the maximum vertical deformations of track slabs are analyzed considering three positive and three negative temperature differences, and the results are listed in Table 10.11.

The results show that the longitudinal connections can reduce the maximum vertical deformations of the track slab at both the positive and negative maximum temperature gradients; the difference between the initial temperature and the slab top temperature has the greater reduction effect than the temperature gradient on the warping deformation, and the bigger the difference, the greater the effect.

3. Dynamic analysis of train-track system under temperature loads

The track deformation under maximum temperature difference 16.2 °C (slab top temperature 52.6 °C, bottom temperature 36.4 °C) shown in Fig. 10.44 is adopted as additional track unevenness, which is added on the original track irregularity, to study the influence of slab temperature warping deformation on bridge track and train running performance. When a CRH2 train with eight vehicles passes through

Table 10.11 Maximum vertical deformations of track slab under various temperature gradients

Temp. effects	Initial temp. (°C)	Final temp. (°C)		Temp. difference (°C)	Max. deformation (mm)		Reduction (%)
		Slab top	Slab bottom		Single slab	Three slabs	
TG3	20	52.6	36.4	16.2	2.89	2.52	12.8
TG4	20	21.6	5.4	16.2	0.7	0.67	5.0
TG5	20	21.6	8.8	12.8	0.53	0.5	4.6
TG6	20	27.6	35.6	−8	0.5	0.47	6.9
TG7	20	30	38	−8	0.53	0.48	8.0
TG8	20	30	35.5	−5.5	0.37	0.32	11.5

Note "TG3" corresponds to the maximum temperature gradient (Fig. 10.40); "TG5" corresponds to "TG2" in Table 10.10; "TG4" corresponds to the positive temperature gradient of "TG3" and the slab top temperature of "TG5"; "TG6" corresponds to the maximum temperature gradient in Fig. 10.44; "TG8" corresponds to the temperature field in Han et al. (Han and Sun 2011); "TG7" corresponds to the negative temperature gradient of "TG6" and the slab top temperature of "TG8"

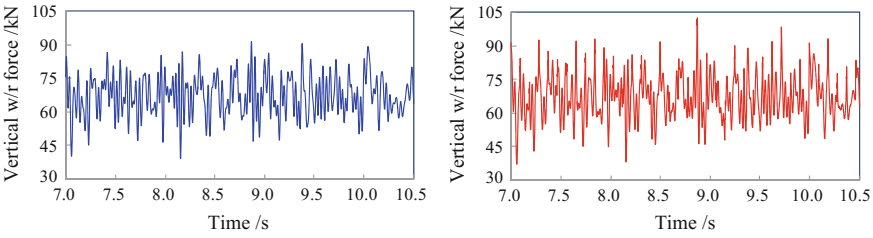

Fig. 10.46 Time histories of vertical wheel-rail forces of vehicle

the normal section and the temperature effect section of the track on the bridge, the dynamic responses, such as the vertical wheel-rail force, the fastener reaction force, the vertical rail acceleration, and slab acceleration, are calculated, and the dynamic response curves are shown in Figs. 10.46, 10.47, 10.48, and 10.49. In the analysis, the fastener stiffness is 22.5 kN/m, the original track irregularity is generated based on the German low interference spectrum, with the wavelength range between 1 m and 80 m, and the train speed of 250 km/h.

It can be seen from the figures that when the train runs on the track section with temperature warping deformation, the time histories of vehicle and track responses

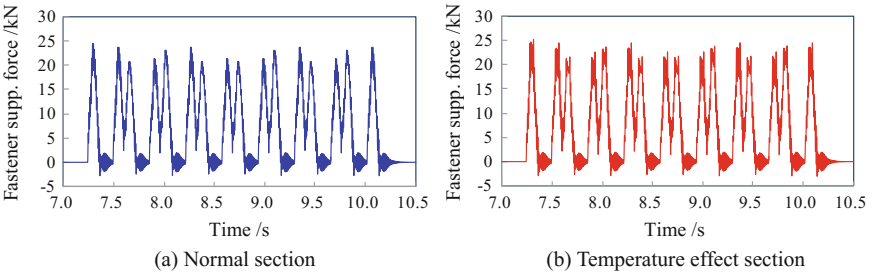

Fig. 10.47 Time histories of fastener support reaction forces

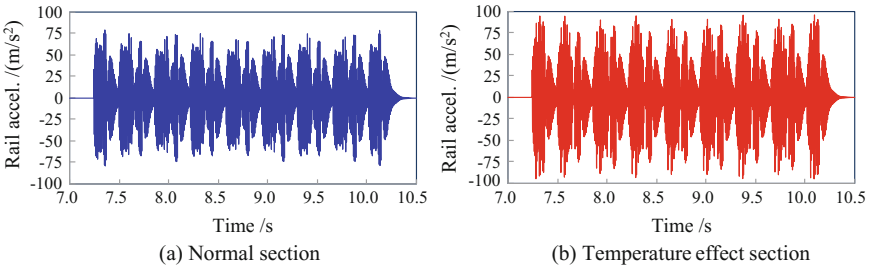

Fig. 10.48 Time histories of vertical rail accelerations

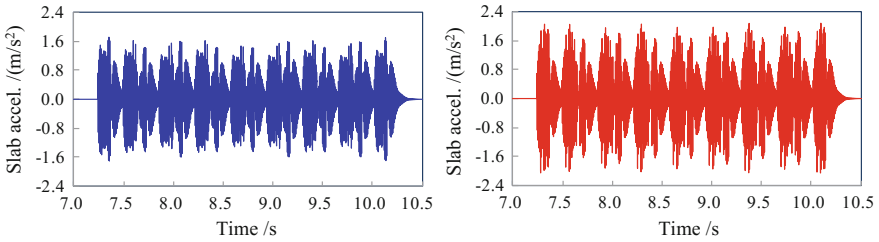

(a) Normal section (b) Temperature effect section

Fig. 10.49 Time histories of vertical slab accelerations

Table 10.12 Maximum dynamic responses of track and train vehicle

Dynamic response	Normal section	Temperature effect section	Increase ratio (%)
Wheel offload factor	0.3	0.318	6.0
Fastener support reaction force (kN)	24.39	25.25	3.5
Maximum vertical rail acceleration (m/s^2)	79.49	95.93	20.7
Maximum vertical slab acceleration (m/s^2)	1.72	2.08	20.7

are similar to those when it runs on the normal section, but the amplitude of the responses are increased.

The maximum dynamic responses of the vehicle and the track caused by the temperature deformation of track slab are listed in Table 10.12, where the responses of them on the normal track section are also given for comparison.

It can be seen that when the temperature deformation of the track slab is considered, the wheel offload factor is increased by 6.0%, the fastener support reaction force is increased by 3.5%, and the vertical accelerations of rail and slab are both increased by so high as 20.7%, which is disadvantageous to the track structure and the train running safety, thus it should be noticed.

References

ACI209 (1992) Prediction of creep, shrinkage and temperature effects in concrete structures [S]. American Concrete Institute committee

AASHTO (2012) LRFD bridge design specifications [S]. In: American association of state highway and transportation officials. Washington, D.C

Bazant ZP, Baweja S (1995) Creep shrinkage prediction model for analysis and design of concrete structures-model B3 [J]. Mater Struct 28:357–365

Bian MZ (2009) Study on temperature and shear lag effect experiment of PC box girder [D]. Chongqing Jiaotong University, Chongqing (in Chinese)

BS5400 (1990) BS5400: Part 4. Code practice for design of concrete bridges [S]. British Standard Institute

CEB-FIP (2010) Model code for concrete structures [S]. Fédération Internationale du Béton

Chai SF (2012) Research on the sensitivity analysis of monitoring and parameter affecting the large span continuous construction of passenger dedicated line [D]. Lanzhou Tiaotong University, Lanzhou (in Chinese)

Chen B, Zheng J, Wang JP (2010) State-of-the-art of the temperature effects of bridges [J]. J Wuhan Univ Technol 32(24):79–83 (in Chinese)

Duan XW (2014) Study on lateral displacement analysis of multiple factors on concrete curved continuous box-girder bridge [D]. Chang'an University, Xi'an (in Chinese)

Gardner NJ, Lockman MJ (2001) Design provisions for drying shrinkage and creep of normal-strength concrete [J]. ACI Mater J 98(2):159–167

Han ZG, Sun L (2011) Temperature measurement and deformation analysis for CRTSII ballastless track slabs [J]. Railw Stand Des 10:41–44 (in Chinese)

He SH (2003) Theory and calculation method of bridge structure [M]. People's Communication press, Beijing, p 2000

He X, Fang SS, Fang F (2012) Analysis of temperature effects of curved bridge under different gradient temperature load [J]. J Hefei Univ Technol (Nat Sci) 35(8):1088–1092 (in Chinese)

He JR (2013) The research on temperature field and temperature effect of the multi-cell concrete box-girder [D]. Hunan University, Changsha (in Chinese)

JTG D62 (2004) Code for design of highway RC and PC bridges and culverts [S]. The ministry of communications of PRC. China Communication Press, Beijing (in Chinese)

JTJ023 (1985) Code for design of highway RC and PC bridges and culverts [S]. The ministry of communications of PRC. China Communication Press, Beijing (in Chinese)

Kyle Buick F (1981) Influence of solar radiation on bridge structure [M]. China Railway Publishing House, Beijing (in Chinese)

Li GQ, Liu XB, Yang F (2014) Variation law and impact on dynamic performance of profile irregularity caused by creep of simply-supported beam on high-speed railway [J]. Sci Sin (Technologica) 44(7):786–792 (in Chinese)

Liu CY, DeWolf JT (2007) Effect of temperature on modal variability of a curved concrete bridge under ambient loads [J]. J Struct EngASCE 133(12):1742–1751

Liu H (2004) Research about lateral displacement and torsional distortion of PC continuous curved box-girder [D]. Southeast University, Nanjing (in Chinese)

Liu Y, Zhao GT (2013) Analysis of early gap between layers of CRTS II slab ballastless track structure [J]. China Railway Science 34(4):1–7 (in Chinese)

Liu Y, Chen P, Zhao GT (2014) Study on the characteristics of early temperature field of CRTS II slab ballastless track structure [J]. China Railway Science 35(1):1–6 (in Chinese)

Liu ZY (2005) Prefabrication and installation of high-speed railway double-track global-span simply-supported box-girder [D]. Southwest Jiaotong University, Chengdu (in Chinese)

Niu B (2008) A summary of China's high speed railway bridges [C]. In: The 18th national bridge academic conference, Changsha (in Chinese)

Priestley MJ (1976) Design thermal gradients for concrete bridges [J]. NZ Eng 31(9):213–219

Priestley MJ (1978) Design of concrete bridges for temperature gradients [J]. J Am Concr Inst 75 (5):209–217

Shan WW (2014) Two-dimensional temperature gradient effects and design methods of curved continuous box girder bridges [D]. Chang'an University, Xi'an (in Chinese)

Sun Q (2013) The temperature effect analysis on high-speed railway simply-supported beams running safety [D]. Beijing Jiaotong University, Beijing (in Chinese)

TB10002.1 (2005) Fundamental code for design on railway bridge and culvert [S]. The ministry of railways of PRC. China Railway Publishing House, Beijing

TB10002.3 (2005) Code for design on reinforced and prestressed concrete structure of railway bridge and culvert [S]. The ministry of railways of PRC. China Railway Publishing House, Beijing (in Chinese)

TB10621 (2014) Code for design of high-speed railway [S]. National railway administration of PRC. China Railway Publishing House, Beijing
Tian Y, Zhang N, Sun Q, Du XT, Xia H (2015) Temperature effect on running performance of steel railway bridge [J]. J Vib Shock 34(12):94–100 (in Chinese)
Wang SR, Sun L, Li QY (2009) Temperature measurement and temperature stress analysis of ballastless track slab [J]. J Railw Eng Soc 2:52–55 (in Chinese)
Xia H (2010) Maintenance and repair of railway bridges [M]. China Railway Publishing House, Beijing
Xia H, Ji WY, Han B, Zhang N (2011) Bridge engineering [M]. Higher Education Press, Beijing
Xia Y, Hao H, Zanardo G et al (2006) Long term vibration monitoring of a RC slab: temperature and humidity effect [J]. Eng Struct 28(3):441–452
Ye MX, Liu J (2009) Experimental research on creep deformation of high strength concrete of no-ballastless-track bridge [J]. J Shihezi Univ 27(1):84–86 (in Chinese)
Zhai WM (2007) Vehicle–track coupling dynamics (third edition) [M]. Science Press, Beijing
Zhang YH (2008) Research and application on shear lag effect and temperature effect theory of box girder bridge [D]. Southwest Jiao Tong University, Chengdu (in Chinese)
Zheng J (2008) High-speed railway bridges in China [M]. Higher Education Press, Beijing